# Designing, optimizing, and testing of a river hydrokinetic prototype turbine system for remote northern communities

by

Raul Vaid

A Thesis Submitted to the Faculty of Graduate Studies of

the University of Manitoba

in Partial Fulfilment of the Requirements of the Degree of

MASTER OF SCIENCE

Department of Mechanical Engineering

The University of Manitoba

Winnipeg, Canada

## Nomenclature

| | |
|---|---|
| $\alpha$ | Turbine yaw angle concerning the mean flow |
| $\beta$ | Buoy force distribution |
| $\theta$ | Angular acceleration of the turbine system |
| $\eta_g$ | Gearbox efficiency |
| $\eta_g$ | Gearbox efficiency |
| $V_H$ | Heavy buoy volume |
| $V_L$ | Light buoy volume |
| $\lambda$ | Tip speed ratio |
| $v$ | Kinematic viscosity |
| $\omega$ | Rotor angular velocity |
| $\rho$ | Water density |
| $\rho_H$ | Density of heavy buoy contents |
| $\rho_L$ | Density of light buoy contents |
| $\theta_t$ | Inclination angle of the turbine system |
| $A$ | Swept blade area |
| $b$ | System's frictional coefficient |
| $C_f^c$ | Counter-torque coefficient concerning torque |
| $C_p$ | Power coefficient |
| $C_r^c$ | Counter-torque coefficient concerning rotor torque |
| $C_t$ | Torque coefficient |
| $D_b$ | Largest diameter of the buoy |
| $F_H$ | Negative buoyant force |

$F_L$ Positive buoyant force

$F_T$ Total force to counter-torque

I Current drawn

$I_m$ Moment of inertia of turbine system

L Spoke arm length

$L_b$ Length of the buoy

$P_f$ Power available in the flow

$P_r$ Power extracted by the rotor

$P_o$ Power output

R Applied load on the generator

r Rotor radius

$R_a$ Armature and commutator resistance

$T_f$ Torque available inflow

$T_g$ Torque output from the gearbox

$T_H$ Heavy buoy counter-torque

$T_L$ Light buoy counter-torque

$T_r$ Torque extracted by the rotor

$T_T$ Total counter-torque

$V_{fs}$ Free stream velocity

$\Delta$ Difference

$\mu$ Dynamic viscosity

**List of tables**

**List of Figures**

**Table of Contents**

# 1. Introduction

## 1.1 Energy mix in remote communities in Canada

In many remote communities across Canada, power is dependent upon diesel generation, as shown in Figure 1 [1]. Diesel power generation has a short fuel delivery window, high costs, environmental risk, does not support community jobs creation, and causes a carbon footprint from its usage. According to the National Oceanic and Atmospheric Administration data, shown in Figure 2, in 2018, the $CO_2$ concentration in the atmosphere at 408 ppm, up from 401 ppm in 2016 an increase of 2% in 2 years while in 1970 $CO_2$ concentration in the atmosphere was at 325 ppm, which is an increase of 25% in 48 years. Under the given global energy mix, $CO_2$ concentration in the atmosphere will cross the critical 500 ppm mark in the next few decades [2]. This high level of anthropogenic $CO_2$ will have decisive repercussions on biodiversity.

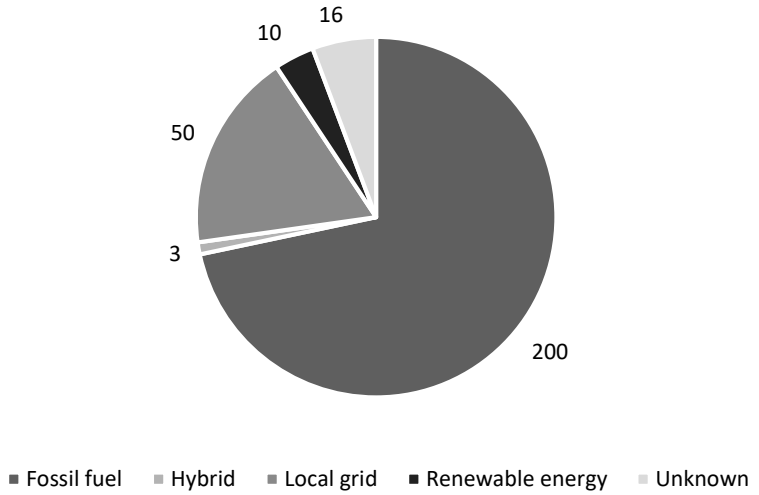


Figure 1: The distribution of primary fuel source to produce electricity in remote communities in Canada.

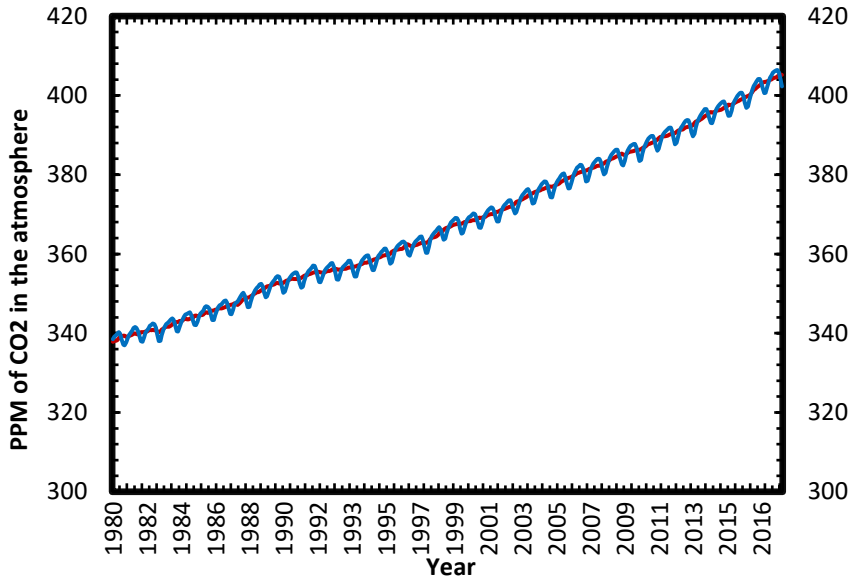


Figure 2: Increase in the amount of CO2 in the atmosphere showing the present-day concentration that exceeds the highest level ever recorded since the advent of mankind. The trend line in shown in red.

In northern Canadian territories, the unsubsidized cost of electricity can exceed 1.1 CAD$/kWh [1]: 0.10 CAD$/kWh [3]–[6] is the average residential electricity cost in Canada. The higher cost of electricity is due to the transportation of diesel fuel, increased handling and distribution of the fuel, lower generation efficiency, shorter amortization of capital, and increased operation and maintenance costs. The 940 GWh produced by fossil fuels for remote communities is federally subsidized on average by 0.70 CAD$/kWh [7], [8]. Apart from the dependence on the transportation of fuel, frequent diesel spills are detrimental to the health of the inhabitants [9]. Developing baseload generators for micro-grids, including the more than 270 remote First Nation communities [1], is critical to provide a viable solution to replacing diesel fuel generation altogether.

## 1.2 Hydrokinetic turbines

Hydrokinetic turbines (HKT) are turbines that extract energy from energetic riverine currents. An HKT comprises of the generator, impeller assembly, support system, control electronics, and power electronics [10]. The impeller assembly comprises the impeller and the shaft, which provides torque to the generator to extract power from river currents. The power electronics continually adjusts the design tip speed ratio of the HKT system. The power varies with the change in river velocity—the power electronics provide the micro-grid with AC power synchronized to the local grid.

HKTs can be categorized based on their position in the water column as shown in Figure 3: bottom-mounted or near-surface. Bottom mounted turbines have their turbine structure in contact with the riverbed. These turbines extract power within the boundary layer region, where the flow is 30% to 60% of the free stream velocity [11]. Figure 4**Error! Reference source not found.** details the specialized barges/pontoons required to aid the deployment and retrieval of the bottom-mounted turbine. Owing to the specialized equipment required, accessing these turbines is difficult even during summer months, resulting in higher maintenance costs.

Moreover, during low winter flows, their proximity to the boundary layer produces less power and can cause the turbine to stall. In contrast, near-surface turbines are mounted on a pontoon assembly to maintain turbine operation in the highest velocity region. However, these systems act as a point of ice accretion in winter, leading to ice build-up. Turbine operation in such conditions risks structural damage and cannot operate in

winter [12]. However, these turbines are more cost-effective to deploy as compared to bottom-mounted turbines, as detailed in Figure 5**Error! Reference source not found.**. Successfully integrating the HKTs into micro-grids would require them to overcome the critical issue of delivering near-rated power in winter months.


Figure 3: Two examples of the types of HKTs tested at the Canadian Hydrokinetic Turbine Test Center showing: a) a near-surface HKT with the rotor located near the maximum free stream velocity, b) bottom mounted HKT with a mounting structure to allow the rotor to rise above the boundary layer, and c) the same turbine operating at the bottom of the river.

Despite the shortcomings of the HKT systems, there are many distinct advantages over other renewable energy sources. These are summarised below [13]–[16] :

- HKTs extract power from a perennial source of energy, i.e., the flow of rivers and tides. Thus, HKTs can displace diesel generators in remote communities as it can provide baseload power.
- These systems are GHG neutral as there is no source of carbon emissions.
- Water is 1,000 times denser than air so HKTs have a higher energy density than wind turbines but are limited on the blade diameter.

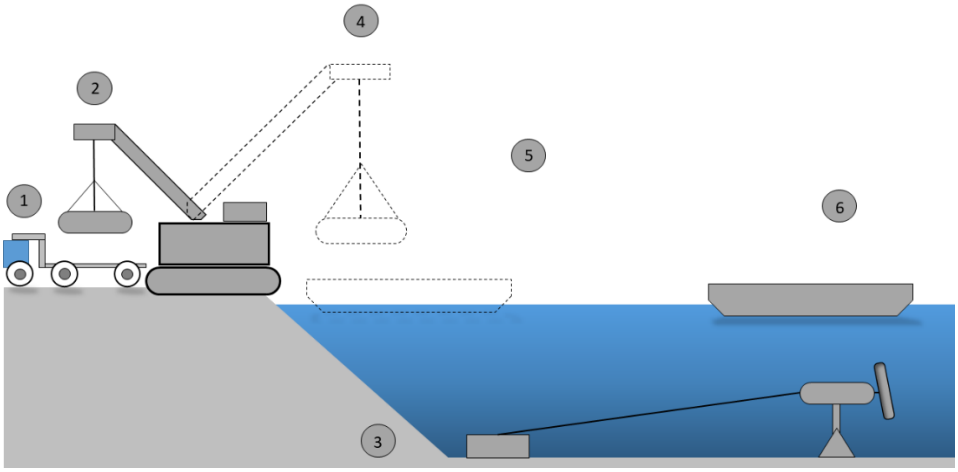


Figure 4: Deployment procedure for bottom mounted HKT. Step 1: Illustrates the generator assembly arriving on-site in a flatbed trailer. Step 2: shows the generator assembly being taken off a flatbed trailer using a crane. Step 3 involves accurately locating the anchoring point. Step 4 shows the turbine being loaded on the specially designed barge. Step 5 shows the transportation to the operational point. Step 6: Show the turbine being lowered and in operation at the bottom of the river.

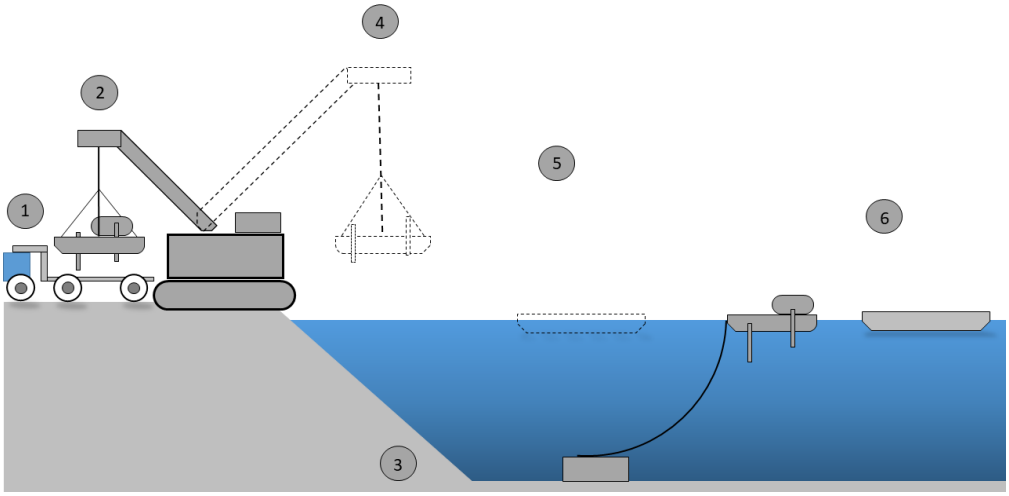


Figure 5: Deployment procedure for near-surface HKT. Step 1: Illustrates the HKT assembly arriving on-site in a flatbed trailer. Step 2: shows the HKT assembly being taken off a flatbed trailer using a crane. Step 3 involves accurately locating the anchoring point. Step 4 shows the turbine floating behind a barge. Step 5 shows the transportation to the operational point. Step 6: Show the turbine being moored and set-up for operation.

Ways to simplify typical deployment and retrieval procedures shown in Figure 5 was investigated in a laboratory water tunnel [17], with a laboratory-scale turbine successfully tested. The focus of this laboratory porotype design was to integrate the

deployment, retrieval and operations into a single system that allows positioning the turbine within the water column. A Counter Torque-Hydrokinetic Turbine (CT-HKT) was tested in a water tunnel and achieved stable operations. It was concluded based on the laboratory results to move forward and develop a river CT-HKT prototype. The scaled CT-HKT laboratory system is shown in Figure 6.

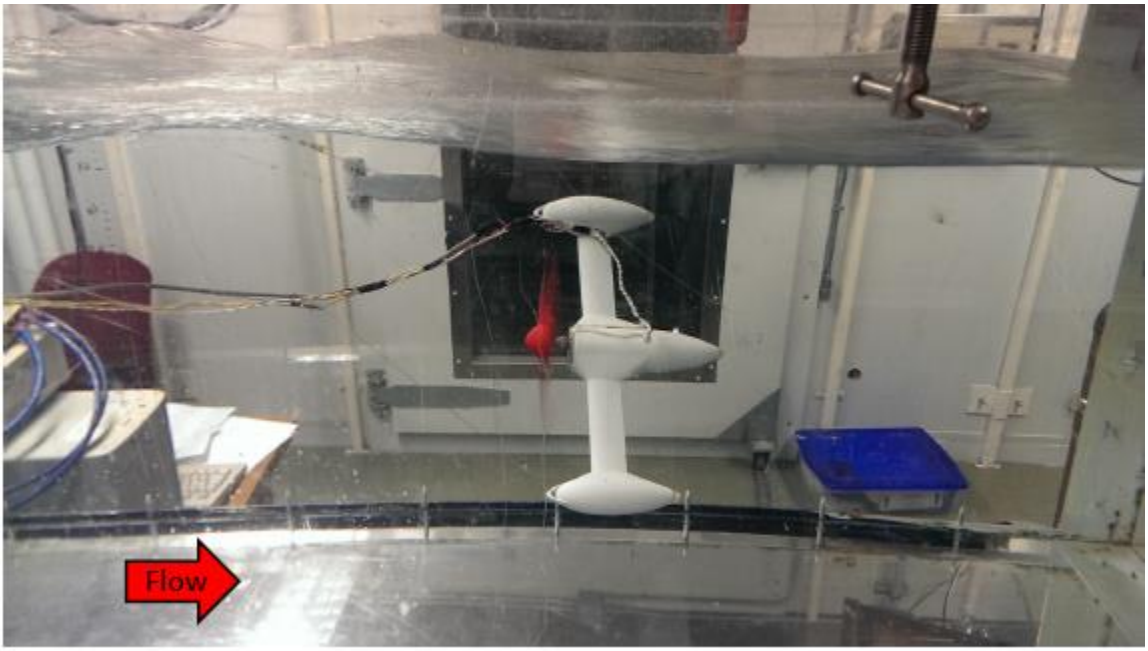


Figure 6: Experimental scale CT-HKT from Reference with counter-torque system with one buoy can be filled with air and the other with water of heavier material providing a passive counter torque system to prevent the turbine to spin around its centerline when the rotor is producing power [17].

## 1.3 Objectives

Considering the potential advantage of CT-HKT to reduce the LCOE? to achieve renewable energy micro-grids in northern remote communities, the objectives are to address HKT winter issues hindering the adoption of HKTs:

- design, manufacture, and test a field prototype of a CT-HKT in a highly energetic

riverine environment, and

- numerically develop add-on components to aid the CT-HKT to produce a given power in low flow winter conditions.

## 1.4 Research methodology

A CT-HKT turbine is required to test in-situ and operate in a highly energetic river system to build upon the previous laboratory-scale model [17]. The methodology is to develop an integrated design and use two approaches:

1) design-build a river turbine prototype using solid modelling (Solid Works) and numerical modelling (Ansys-CFD),

2) test the CT-HKT prototype in-situ the at an HKT test facility (CHTTC), and

3) perform numerical modelling to optimize the seasonal components to add to the turbine to address low flow issues (Ansys-CFX).

The design of the CT-HKT requires integrating many design components to achieve research objectives. The turbine nacelle requires considering the rotor and generator in combination. Generator selection is made based on design target power, RPM, torque, and weight. The rotor design is two-bladed to be able to float the turbine near the riverbank during deployment in less than 1 m of water depth to significantly reduce the cost of deployments by allowing a trailered deployment. Additionally, the rotor was

designed to be 3-D printable with reinforcement rods. The turbine design is integrated to include transportation to site, deployment, operation, and retrieval. Functional components need to allow the CT-HKT system to position itself in the water column by changing buoyancy. As part of the design methodology, the turbine prototype needs to have positive buoyancy during the deployment and retrieval phases. The system needs to achieve negative buoyancy to allow it to achieve its operational depth. Once the system reaches its location in the water column, the turbine is made neutrally buoyant. While in the operational state, the turbine needs to counter-balance the rotor torque. A passive counter-torque force is necessary for the CT-HKT to achieve stable operation. The passive counter-torque needed to produce rated power is based upon the wingspan of the turbine, positive buoyant force, and the negative buoyant force exerted by the cavities on either side. Additionally, the CT-HKT needs to address ice issues and low flow conditions to achieve research objectives. The methodology to address icing issues is to move the turbine vertically within the water column. The turbine design includes seasonal add-on components to counter address low flow conditions. The add-on seasonal components identified were shrouds, winglets, and wingtips. To test the performance of seasonal components, Ansys-CFD simulations is used. Figure 7 shows a diagram of the methodology employed to achieve research objectives.

## 1.5 The relevance of the research and contribution

Northern climates in Canada are not suitable for operations of near-surface HKTs because of adverse cold weather conditions [12]. While in many parts of the world during summer months, the rate of flow of rivers is decreased, in Canada the flow decreases

in winter while the load demand increases. The key to HKTs as a viable micro-grid electricity generation option would require the turbine to be below the surface in sub-zero winter conditions and not positioned in the bed boundary layer. The contribution of this research will encourage the adoption rates of HKTs for energy production purposes while lowering the Levelized Cost of Energy (LCOE) for the technology. Specially designed add-on seasonal components can counter the detrimental effect on LCOE during low flow conditions. A higher adoption rate for HKTs would lead to more investments both by governments and private entities in the marine industry. This investment would drive costs further down as there would be more large-scale production and more resources to improve the technology further [18]. Potential lower costs and access to a reliable source of base load power would further promote renewable energy micro-grids in remote communities.

This research investigates a new approach of extracting power from the free stream of a highly energetic river in low flow and cold weather. It also combines deployment, retrieval, and power generation into an integrated unit to eliminate dependency on specialized equipment and reduce variations in deployment approaches. Being able to deploy in shallow riverbanks contributes to further reduce the LCOE.

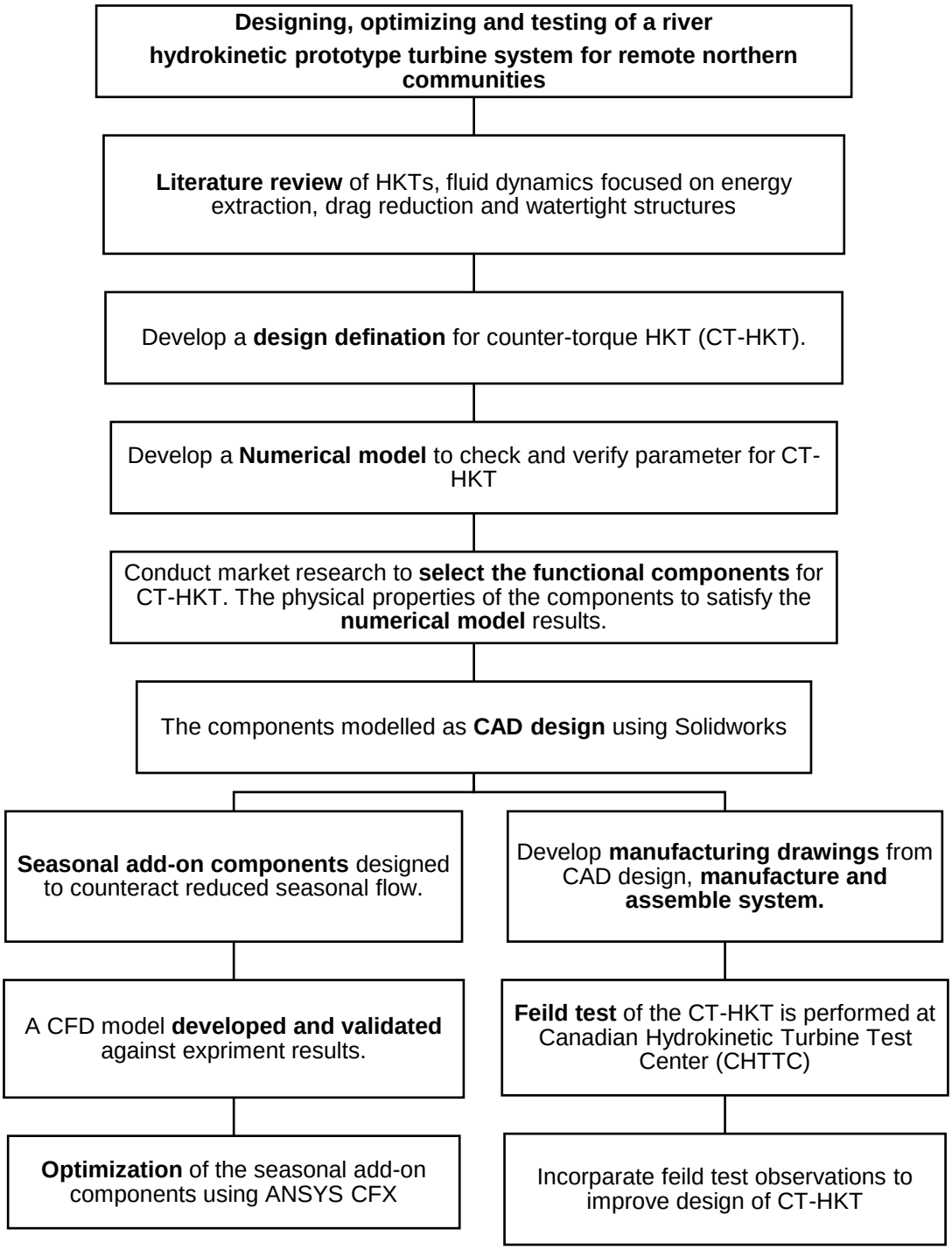


Figure 7: Research methodology used to achieve research objectives: Solid Works is used to design the turbine and calculate center of mass and center of buoyancy; Matlab is used to calculated counter torque; and Ansys-CFD and optimization is used to design the two-blade rotor, shroud and winglets.

## 2. Literature review

In order to better understand how remote communities in cold climates can reduce their dependence on fossil fuels using the proposed CT-HKT system, it is required to review the literature on the HKT resource in northern Canada and determine how to address previous failures in cold climates of these turbines. In addition, development of the proposed CT-HKT system for remote communities requires adding components to address the reduced flow rates in winter. These components require reviewing performance-enhancing elements used in the wind and aviation industry. Numerical models used to rank the performance of selected components also require reviewing to select the appropriate turbulence model for rating add-on components.

### 2.1 Resource characterization

Resource characterization in remote location is critical for the application of year-round operations of the CT-HKT in micro-grids, as riverine HKT technologies operate in highly energetic river systems. The ability to characterise these energetic river systems is central for the development and long-term operation of HKT. Attempts have been undertaken to characterise North American river systems and develop tools to improve the accuracy of characterisation by using existing highly granular data. For example, HKT assessments have been conducted across Canada [19]. The study is based on the hydro-climatological data and topographic map data. The study assumed multiple hundreds of kilometres of uniform reach, the channel roughness geometry, a uniform turbine efficiency of 40%, average widths determined manually from national topographic maps, and channel slopes. The study was restricted to larger rivers in

Canada. River reaches inclusion was limited to flow rates of less than 450 $m^3/s$, velocities less than 1.5 m/s, width less than 50 m, depth values less than 3 m, and monthly mean flows were studied in power estimation. The study presents results illustrated by cross-sectional bars for each analysed river segment. Table 1 emphasises results from the report; the overview of results from the report is shown in Figure 8.

Table 1: Highlights the noteworthy results from Reference [19].

| River name | Number of regions the river was divided into | Notable observation |
|---|---|---|
| Mackenzie | 17 | The highest energy density calculated at 3 $kW/m^2$ |
| Fraser | 9 | 5 regions with an energy density higher than 12.5 $kW/m^2$ |
| Slave | 5 | 2 regions with an energy density higher than 1.5 $kW/m^2$ |

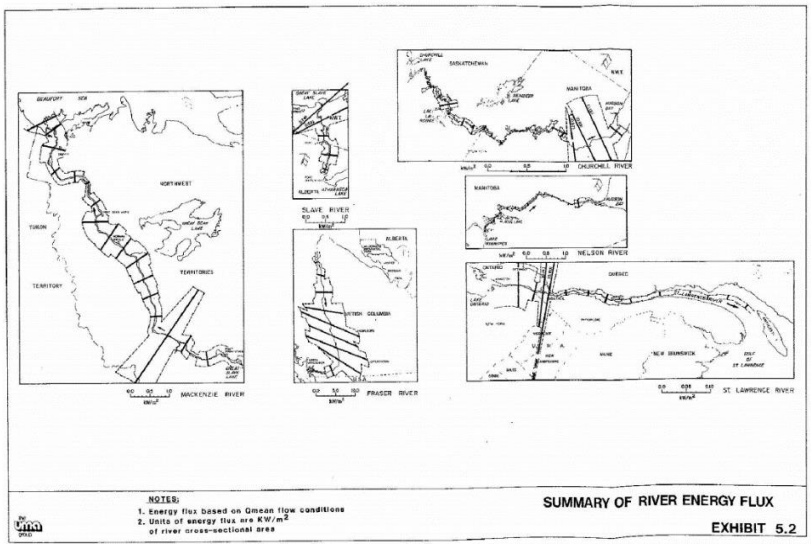


Figure 8: Results from Reference [19] report showing the coarse HKT energy available in Mackenzie, Fraser, Slave, Churchill, Nelson, and St. Lawrence rivers. The lack of a singular HKT potential value is because of the methods and data available.

United States Department of Energy also conducted a study to assess the HKT potential

in the United States [20]. They divided the continental US into 16 hydrologic regions and restricted their data analysis to rivers with flow rate greater than 113 $m^3/s$ and bulk flow velocities greater than 1.3 m/s. Channel slopes and geometry were estimated similar to Reference [19] and the river velocity was approximated using manning equation [21]. The total resource potential was calculated by assuming the turbines can occupy up to 25% of the width of the rivers, have a diameter of 80% of the mean depth, are staggered with a 0.5 diameter distance across the width of the river, the downstream distance between the turbines is five diameter and the capacity factor for the turbines is set at 40%. The reported HKT potential was 12.5 GW, with the bulk focused in the western and northwest of the US and in the state of Alaska. In contrast, Bomhof using concepts from the NRC-2008 study predicted that Canada has an HKT power potential of 340 GW [19], [22], [23].The provincial distribution of calculated power is given in Table 2. Bomhof based the model on velocity derived from flow rate and geometries of the channel, thus not accounting for sudden elevation changes occurring at the Canadian Rockies. The study points out that lack of data from the northern territories causes under-predicting the HKT potential [23].

In 2014, the Canadian Hydrokinetic Turbine Test Center (CHTTC) started a campaign to collect flow measurements along the Winnipeg River. This campaign, to date, has measured 48 points over 176 km of the 235 km long river, shown in Figure 9. d'Auteuil et al. identified the selected points as a part of a previous project, focused on identifying the ice openings present in an otherwise frozen river [11]. The sites selected can sustain HKTs throughout the year. The CHTTC collected the measurements following the near-

surface measurement procedure [24]. The near-surface measurements were recorded using Nortek Acoustic Doppler Velocimeter (ADV) at a depth of 1.2 m. The recorded data is post-processed utilising, a “despike” routine to remove electronic and signal noise [25]. The average velocity from the post-processed data is used to determine the power potential at each location. Next, a World Bank report states remote communities such as the RM of Alexander, RM of Lac du Bonnet, Pinawa, and Sagkeeng First Nation have a total annual average residential energy consumption of 35 GWh [26]. Commercial HKT can produce power over water velocities of 1.5 m/s. The data analysis from the campaign observed that a single point could produce an annual maximum of 13 MWh/$m^2$ [27].

Table 2: Bomhof calculated HKT power in Canada by Province.

| **Province and Territory** | **HKT power (GW)** |
|---|---|
| Prince Edward Island | 0.016 |
| Nova Scotia | 0.59 |
| New Brunswick | 3.8 |
| Nunavut | 7.3 |
| Saskatchewan | 7.4 |
| Yukon | 20 |
| Newfoundland and Labrador | 20 |
| Alberta | 22 |
| Manitoba | 28 |
| Ontario | 42 |
| British Columbia | 45 |
| Northwest Territories | 73 |
| Quebec | 74 |

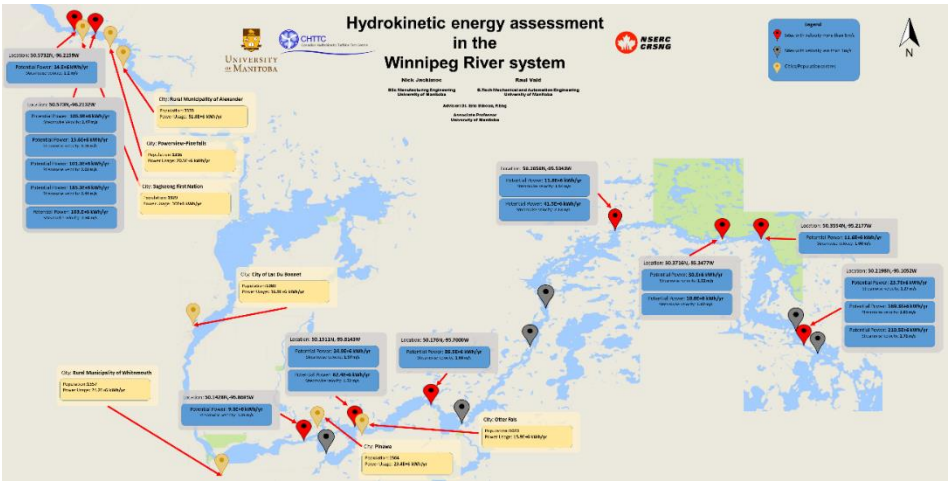


Figure 9: For potential satellite locations identified, 16 locations or 1/3 of the locations were identified as being suitable for HKT deployment.

## 2.2 Problems inhibiting the adoption of HKTs

The literature documents issues that restrict the adoption of HKTs. This includes damage to the floatation system because of ice formation during sub-zero temperatures, expensive deployment and retrieval procedures, and performance loss due positioning of HKT onto the riverbed. These factors increase the LCOE defined as [11], [12], [28]–[31]:

$$LCOE = \frac{\sum_{t=1}^{n} \frac{I_t + M_t + F_t}{(1+r)^t}}{\sum_{t=1}^{n} \frac{E_t}{(1+r)^t}} \quad (1)$$

where

$L_t$ – Capital Investment in the project in year t

$M_t$ – Operational and Maintenance costs in year t

$F_t$ – External Fuel costs in year t

$E_t$ – Electricity generation in year t

r – Discount rate

n – Life of the system

t - Time in years

HKTs in contact with air above the water surface leads to ice accretion around the HKT structure that can damage the flotation system causing the HKT system to sink [12], [32]. Studies by Kassam et al. show that ice formation occurs below the surface due to frazil ice causing a build-up of frazil in front of the turbine and sub-zero temperatures affecting the gearbox fluid viscosity [12], [33]–[36]. The formation of ice on structures in contact with air, as shown in
Figure 10, adds new loads to the mooring lines that eventually sink the turbine. These issues lead to a much higher LCOE.

Furthermore, the velocity profile in rivers has the boundary layer form an energetic region away from the riverbed. The velocity profile in Figure 11 is a non-dimensionalised average of 40 measurements collected by the CHTTC showing that the river surface is 95% of the free-stream velocity, and 35% depth corresponds to the free-stream velocity. Velocity available for near surface HKT is approximately 0.85 of $V_{max}$. In contrast, the velocity available for bottom mounted HKT is 0.6 of $V_{max}$. Figure 11underlines the 33% power advantage that near-surface HKTs have over the bottom-mounted HKTs. Apart from the velocity profile, velocity over time is a key factor to optimise the energy extracted at a site. The CHTTC recorded instantaneous velocity over 104 hours.
Figure 12 shows the variation from the average velocity where the average velocity is 1.2 m/s with velocities ranging from 0.7 m/s to 1.9 m/s. From
Figure 12, the maximum power available per $m^2$ is 3,419 W with 59% of the available power that can be extracted due to Betz limit [37].

Turbulence can increase the velocity in a localized region up to a factor of 3, thus aiding

the HKT to produce more power than the average free stream velocity at that location [38]. Turbulence causes sustained vibrations to the system, which reduces the lifespan of components and cause them to fail prematurely [39], [40]. To mitigate the risk of failures at highly turbulent sites, maintenance checks and load factors must be increased, adding to the LCOE.

Figure 10: Ice accretion around a near-surface HKT. This can cause structural damages to the HKT. The damage can also cause the floatation system to malfunction or break entirely causing the HKT to sink.

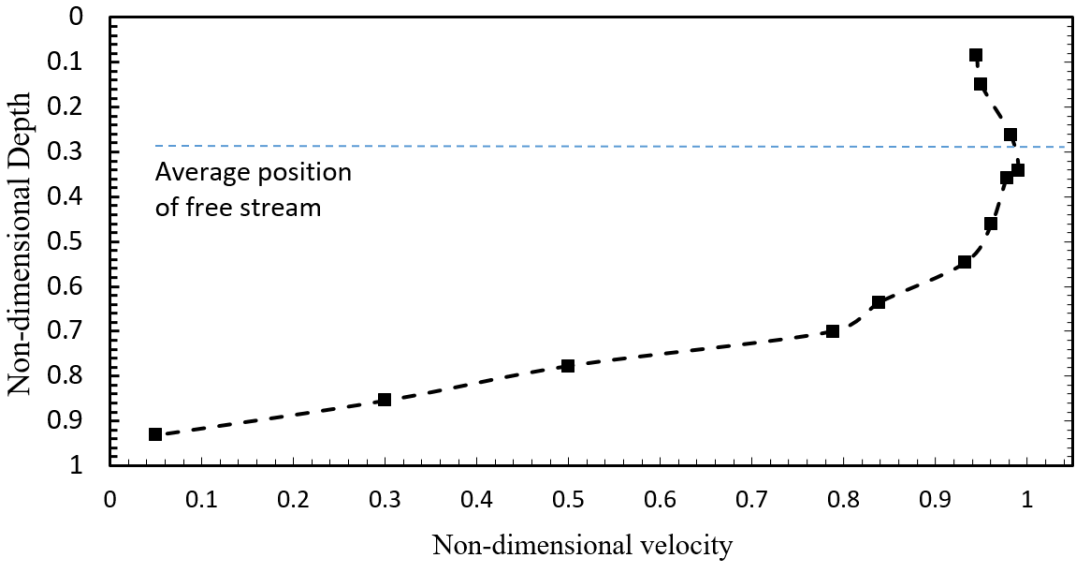


Figure 11: Velocity profile measured at the CHTTC non-dimensionalised and averaged over 40 measurements.

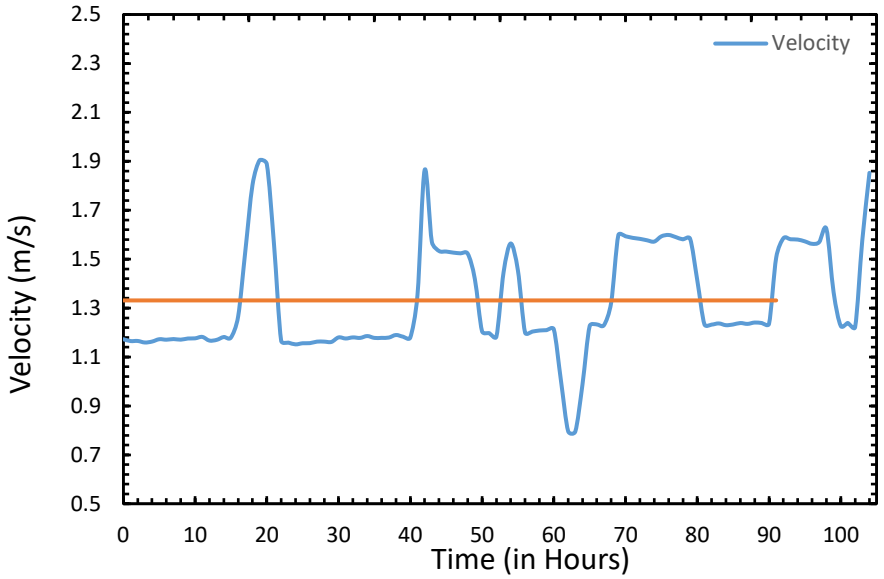


Figure 12: Variation in flow velocities recorded at the CHTTC. The plot shows velocities ranging from 0.7 m/s to 1.9 m/s. The graph also illustrates the importance of instantaneous data over averaged data. The graph shows the average velocity at 1.3 m/s, while the most probable velocity is recorded at 1.2 m/s

Case studies on costs incurred during the lifetime of a bottom mounted tidal turbine and a near surface HKT are detailed below:

The RM1 turbine is inspired by “SeaGen” design, which is a mono-pile mounted dual-motor axial tidal turbine [41], [42]. The RM1 turbine has a neutrally buoyant cross arm to allow for easier access to the dual motor set up for maintenance procedures. Figure 13 renders an operational view of the turbine.

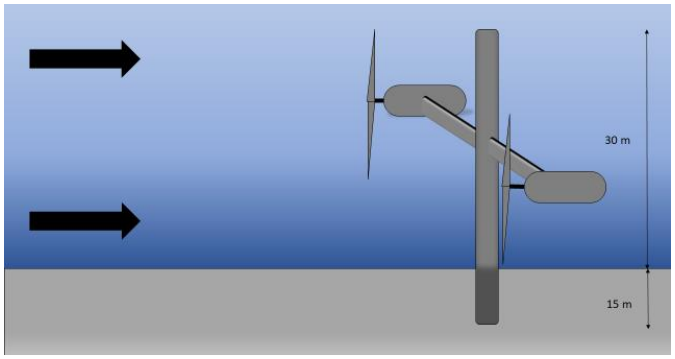

Figure 13: The RM1 turbine. Has the pile driven 15 m below the sea floor and rising 30 m above the sea floor. The blades on the turbine always face the direction of the flow to produce power.

The LCOE of energy for a ten RM1 turbine array is 40.7 ¢/kwh [41]. The report bases this estimate on fixed charge rate, annual energy production, capital expenditure, and operation expenditure. The highest cost during the life of the project is that of manufacturing and development at 21.7 ¢/kWh, followed by the cost of maintenance at 12.2 ¢/kWh. Figure 14 illustrates the other costs contributing to the LCOE of the turbine array.

Sandia National Laboratories assessed the LCOE of a single turbine at 8,250 $/kW. In contrast, the LCOE for a ten-turbine array drops to 1,100 $/kW, which further decreases to 360 $/kW for a 100-array configuration [41]. This reduction in LCOE is because of the optimal utilization of specialized equipment such as the 500-tonne crane barge with RM1, the development costs, and the site characterization costs get split evenly in all the turbines. Maintenance requires a 500-tonne barge to transit to and from the site. Sandia National Laboratories quotes the cost of transportation of 500-tonne barge at $165,536. The cost does not increase with an increase in the number of turbines.

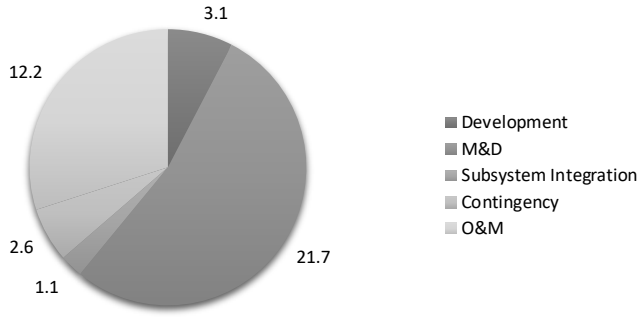


Figure 14: The distribution of LCOE costs involved in the lifetime of one RM1 style turbine. The manufacturing and deployment costs are 21.7 ¢/kWh which can be reduced by spreading it over multiple turbines in the same location.

RM2 is a near-surface turbine inspired by the New Energy Corporation's "EnCurrent Power Generation" turbine [43]. The RM2 turbine is a pontoon-mounted dual turbine system reducing costs involved during manufacturing and deployment [41]. Figure 15 shows how the turbine would look during the operation stage.

Figure 15: The illustration shows the operating state of the RM2 turbine. The turbine is installed on a floating platform allowing the turbine to extract power from the faster moving flow by being closer to the free stream. The single floating platform houses two power producing units with individual impeller assembly. This kind of turbine have been known to be inoperable in extreme winter conditions.

The LCOE for a 10 RM2 turbine array is 80.3 ¢/kWh. The report bases this estimate on fixed charge rate, annual energy production, capital expenditure, and operation

expenditure. the highest cost during the life of the project is that of manufacturing and development at 36.3 ¢/kWh, followed by the cost of maintenance at 25.0 ¢/kWh. The Figure 16 illustrates the other costs contributing to the LCOE of the 10-turbine array.

Sandia National Laboratories assessed the cost of deployment of a single turbine at 5,180 $/kW, while for the 10-turbine array, they evaluate the LCOE at 750 $/kW. The LCOE for a 100-array scale 300 $/kW. This reduction in LCOE is because of the optimal utilization of boats used to toe the turbine RM2 to the site of deployment [41].

A summary between near-surface and bottom mounted HKT is given in Table 3.

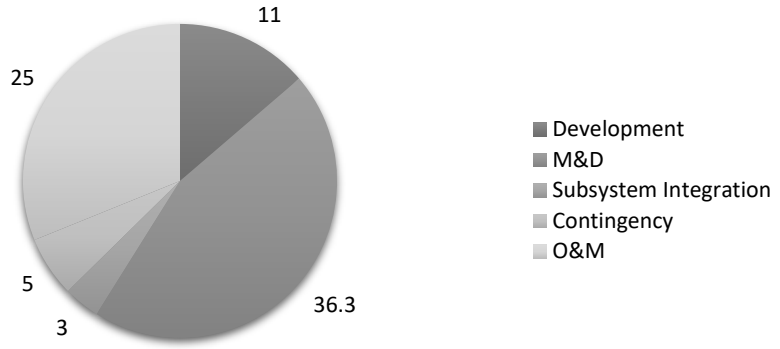


Figure 16: The distribution of LCOE costs involved in the lifetime of one RM2 style turbine. The manufacturing and deployment costs are 25 ¢ /kwh.

Table 3: A comparison between near-surface and bottom-mounted turbines in terms of normalised velocity free-stream.

| **Factors** | **Near Surface-mounted turbines (RM2-type turbines)** | **Bottom-Mounted turbine (RM1-type turbines)** |
|---|---|---|
| **Velocity at Optimized height for maximum power** | 0.9 Vmax | 0.5 Vmax |

| | | |
|---|---|---|
| **Cost of deployment, retrieval, and maintenance** | Less expensive due to deployed procedures akin to a boat | More expensive due to a need for special equipment |
| **Winter operability** | Cannot operate in winter | Can operate in winter |

## 2.3 Commercially available HKTs

Tropical regions do not record sub-zero temperatures, thus eliminating the risk of damage caused by the ice formation to near-surface HKTs. The lack of sub-zero temperatures allows for the HKT to operate year-round at 80% of the free stream velocity (Vmax). Tropical regions get monsoon rains which results in sudden increase in the mass flow rate of the river system leading to faster flows and debris. Table 4 shows the various HKTs tested around the world.

Table 4: The details of various HKT along with regions of operation, theoretical winter operability, position in the water column, and know or possible issues that could plague the turbine if it were to operate in cold environments have been summarised.

| Name | Capacity | Position in the water column | Max velocity | Theoretical winter operability | Known prospective issues |
|---|---|---|---|---|---|
| **Aquantis Ocean Current Generation Device [45]** | 2.5 MW | Tethered with no real-time adjustment | Vmax | Yes | Always requires the dual rotor assembly to function. If either rotor fails, the turbine assembly would become unstable and would cease to operate |
| **Bluewater's Tidal Energy Converter (BlueTEC) [46]** | 2 MW | Near-Surface | 0.8 Vmax | No | Winter icing can cause the system to fail during sub-zero temperatures |

| Name | Capacity | Position in the water column | Max velocity | Theoretical winter operability | Known prospective issues |
|---|---|---|---|---|---|
| **CoRMat [47]** | 500 kW | Tethered with real-time buoyancy adjustment | Vmax | Yes | Always requires the dual rotor assembly to function. If either rotor fails, the turbine assembly would become unstable and would cease to operate |
| **Deep Green [48]** | 500 kW | Tethered with real-time buoyancy adjustment | Vmax | Yes | Information not available |
| **River-Star [49]** | 50 kW | Near-Surface | 0.8 Vmax | No | Winter icing can cause the system to fail during sub-zero temperatures |
| **Oceade [50]** | 1 MW | Bottom-Mounted | 0.6 Vmax | Yes | Theoretically, the turbine can perform in winter conditions, because of low flow conditions the turbine is prone to stalling |
| **Delta Stream [51]** | 1.2 MW | Bottom-Mounted | 0.6 Vmax | Yes | Known Reliability Issues |
| **Evopod [52] [53]** | 35 kW | Near-Surface | 0.8 Vmax | No | Winter icing can cause the system to fail during sub-zero temperatures |
| **THOR [54]** | 1:50 Lab Prototype | Tethered with real-time buoyancy adjustment | Vmax | Yes | Not enough data available |
| **Tocardo - T1 [55]** | 2 MW | Near-surface | 0.7 Vmax | No | Winter icing can cause the system to fail during sub-zero temperatures |

| Name | Capacity | Position in the water column | Max velocity | Theoretical winter operability | Known prospective issues |
|---|---|---|---|---|---|
| **Tocardo - T2 [56]** | 1.4 MW | Near-surface | 0.7 Vmax | No | Winter icing can cause the system to fail during sub-zero temperatures |
| **GEM [57]** | 100 kW | Tethered with real-time buoyancy adjustment | Vmax | Yes | Always requires the dual rotor assembly to function. If either rotor fails, the turbine assembly would become unstable and would cease to operate |
| **Verdant Powers Kinetic Hydropower System (KHPS) [58]** | 1.3 kW | Bottom mounted | 0.6 Vmax | Yes | Theoretically, the turbine can perform in winter conditions, because of low flow conditions the turbine is prone to stalling |
| **Hydra Tidal [59]** | 1.5 MW | Near-surface | 0.8 Vmax | No | Winter icing can cause the system to fail during sub-zero temperatures |
| **New Energy Corporation [43]** | 20 kW | Near-surface | 0.8 Vmax | No | Winter icing can cause the system to fail during sub-zero temperatures |
| **Clean Current [13]** | NA | Bottom mounted | 0.6 Vmax | Yes | High cost of maintenance and deployment |
| **GEM [57]** | NA | Near-surface | 0.8 Vmax | No | Winter icing can cause the system to fail during sub-zero temperatures |
| **Armin Turbine [29]** | Lab Prototype | Tethered without any control system | Vmax | Yes | Development of suitable control systems can lead to year-round operability |

Higher flows aid in performance of HKTs as established in Section 2.2. However, due to engineering limits, higher than rated flow velocities can lead to overheating of generator winding, causing damage to the generator [60]. In comparison, wind turbines in high velocity conditions modulate the angle of attack for the blades to spill power to maintain rated power conditions. This can be applied to river hydrokinetic turbines passively by having the blade deform at higher velocities. It is also possible to produce rated power by moving the HKT closer to the boundary layer region during high river flows like during monsoons.

HKT systems based on two rotors for counter torque and system stability must be shut down even when a single rotor failure occurs [45], [47], [57]. The concept like RM-2 mentioned in Section 2.2 is a known method to extract energy from the flow of an energetic river [43], [46], [49], [52], [53], [55]–[57], [59]. The introduction of near-surface HKTs such as RM- 2 in a highly energetic river aids in ice formation during sub-zero temperatures, which may result in sinking of HKT system. Armin et al. [29] tested CT-HKT as a laboratory prototype to show the counter-torque capability of the HKT system. The CT-HKT system was 3D printed out of ABS plastic and used a set of metal balls, added manually to alter the buoyancy of the HKT system. In a riverine environment altering buoyancy would require a real-time buoyancy control system. Also, the CT-HKT system would have to do away with the metal balls for buoyancy control. This CT-HKT system promises ease of deployment and retrieval thereby substantially reducing involved cost. The savings in cost of deployment and retrieval provides incentive to further enhance the performance of CT-HKTs to improve LCOE.

## 2.4 Performance-enhancing methods

The CT-HKT objectives look at adding performance enhancements in wintertime to compensate for the lower velocities. The literature discusses add-on components for wind-turbine blades is sparse owing to diminishing returns on investment and the large size of the turbine blades. The estimated wind power potential is 48,000 GW capacity with 597 GW [61] wind generation capacity was installed in 2018. The Off-Shore Energy Research Association states wind turbines already operate at a capacity factor of 0.41, 85% of the time. Therefore, a large untapped wind potential can be exploited through existing wind turbine design. Table 5 summarises the studies of add-on parts that can be retrofitted in sub-sonic flows to enhance performance. The studies outline the increase in the power production of wind turbines, lift produced on an air foil section, reduction of drag, and effects of increased pressure on loading characteristics. In some of these studies, CFD analysis of shrouded wind-turbines has demonstrated an increase in power between 5% to 9%.The trade-off between R&D, costs, and marginal increase in per unit power is not substantial, thereby limiting adoption of these power enhancement devices for wind turbines. CFD analysis of winglets on wind-turbines shows an increase of power from 2% to 20% on a case by case basis. Winglets are known to reduce vibrations on wind turbines and aid in increasing pressure per unit length of the blade to produce more torque. Shahsavarifard and Bibeau [62] showed that performance enhancement shrouds can be easily replaced by extending the rotor blade size at a fraction of the material requirement and costs for HKT.

Table 5: Summary of add-on enhancement for wind turbines

| Author | Type of study | Aerodynamic surfaces/properties tested | Inc. Factor | Test Speed |
|---|---|---|---|---|
| Aniket Aranake [63] | CFD- Rans | S1223 | 3.39P | 5 m/s |
| | | NACA 0006 | 1.93P | |
| Yuji Ohya [65] | Experimental | Shroud shape | 4-5P | 12 m/s |
| Peigang Yan [66] | CFX | One stage shroud | 66-73% | 2 - 6 m/s |
| Shun Yen [67] | Winglet | Lift-drag ratio at stalling conditions | 32%-17% | na |
| NASA [68] | Winglet | Lift drag | 9% | na |
| | Wingtip Extension | Lift drag | >4% | na |
| NASA, Stuart G [69] | Winglet | Drag Reduction | -0.0015 | na |
| | | Loading | 1.40% | na |
| PD Gall [70] | Winglet | Lift drag | 6.40% | na |

In comparison, adoption of a shroud to an HKT system can increase the flow velocity by factor of 1.3 thereby improving the output considerably. The performance of the HKT can be further improved by applying the winglets to the blades of the HKT as they have a similar effect as seen in wind turbines. It is well known that increased fluid density leads to increased vibrations. Therefore, vibrations encountered by a blade would be magnified in water. Thus, inclusion of winglets is advantageous in a denser fluid as vibrations will dampened. Shahsavarifard and Bibeau [62] discusses that for HKT, adding components can have an advantage for the powertrain design and for river turbines. Such approach can prove potentially beneficial if well-conceived.

## 2.5 Blade design methods

To achieve the research objectives, the CT-HKT requires a two-bladed design, uncommon in the marine energy applications. A HKT blade can be divided into three

parts: root, lift region and rotor tip region. Due to the varied functions of the different parts of HKT blade, different geometries are needed for each part. There are various methods in the literature that demonstrate techniques to design a blade for a given operational condition using aerofoil sections. The outline for some of these techniques is mentioned below.

The blade element theory based on 2D study assumes that 100% of the swept area is a solid disc. The theory over predicts power production, fails to predict pressure distribution, and does not resolve post flow regimes. Blade element theory needs to be integrated with Euler hydraulic equations and Navier-Stokes methods [71].

The blade element momentum theory is commonly used for performance analysis in the design of turbine blades. In the past, blade element momentum theory has been shown to under-predict power by 25%, or even over-predict power by 75% in no-stall no-yaw steady-state conditions. A further divergence was found in blade-bending and power produced in stall conditions. However, in 1998 and again in 2005 the accuracy of the theory was tested at NASA's Ames wind tunnel and the results matched experimental data. The improvement in accuracy of the results was due to an accurate representation of the blade aerofoil profile, along with additional data available at the appropriate Reynolds number, including the stall region. The tip loss factor is an add-on to the basic Blade Element Momentum theory and is used to explain lack of power generated due to pressure distribution at the tip of the blade [72].

The Navier-Stokes solution theory predicts forces acting on a blade with accuracy without pre-programmed aerofoil properties and resolves the flow regime up and downstream of the turbine blade. The theory models near-wake and far-wake regions using the eddy viscosity model and large eddy simulation, respectively to provide accurate results. The use of select turbulence models and the proper scale of meshing do away with the need for a tip-loss factor. However, this approach is computationally intensive and very time-consuming [73].

The hybrid model uses the advantages of robustness and accuracy afforded by the of Reynolds-Averaged Navier–Stokes equations model in the vicious region near the rotating blade. The region outside the vicious flow regime is stationary, and potential flow solvers are used to resolve this volume and Lagrangian fluid mechanics scheme for capturing tip vortices [73], [74].

Losses in blade deign are also important to address. Clifton-Smith [75] conducted studies in two cases on a 3-blade wind turbine operating at 10 m/s with a radius of 1.5 m. The study concluded that tip losses could remove up to 7% capacity factor. The capacity factor for a wind turbine, according to U.S. Energy Information Administration, averaged at 34.6% for the years 2017 and 2018 [76]. Further, Khchine et al. [77] mathematically recorded that the last 5th of a turbine blade loses 1/3rd of the torque when compared to the rest of the blade. Studies done involving wind turbines by Vermeera et al. and Helmis et al. [78], [79] highlight that near wake region can extend

5 rotor diameters downstream, with intermediate wake region extending 15 rotor diameters downstream as reported by Hojstrup [80].

Cheon et al. [81] showed experimentally that in the case of wind turbines, winglets with a height to span ratio of 1.36% stopped pressure leakage due to the tip effects on a blade.

A wind turbine has a sophisticated gearbox, a low-speed rotating shaft, and a variable speed and loading during operation. These elements induce vibration. Studies done by Madsen et al. [82] show that vibrations can cause structural damage to the blades in the case of wind turbines. However, this is still an active area of research.

## 2.6 Drag coefficient

To achieve research objectives, it is required to reduce the drag of the two floats of the CT-HKT. NASA quantified the drag coefficient resulting due to different basic shapes and their combinations. A shape projecting a semi-circle followed by a cylinder was found to be the least resistant with a drag coefficient of 0.295. The value of the drag coefficient for aerofoil in a subsonic wind tunnel was recorded to be 0.045. The drag coefficient is dependent on Reynolds number and can change by altering the downstream geometry [83].

An envelope was developed and is referred to as GNVR for low drag airship [84]. The shape is made up of three sections, namely ellipse, circle, and parabola shown in Figure

17. The drag coefficient for the 1st iteration of GNVR shape was calculated at 0.02686; the second iteration saw the drag coefficient fall by 15.8% to 0.0226. The geometry was designed to operate at Mach 0.1 at height of 1 km. The geometry was optimized using a parametrized envelop.

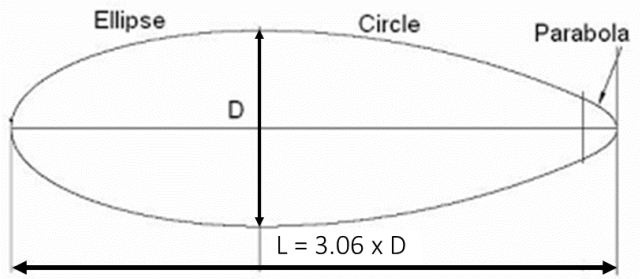


Figure 17: Elements of shape depicting the relationship between diameter of the buoy (D) and length of the buoy (L) as presented in Reference [84].

## 2.7 Control systems using ballasts and buoyancy for airships

Blimps or untethered aerostats form a starting point for the CT-HKT control system because they are piloted objects employing buoyancy control. Gonzalez et al. [85] used a fuzzy controller for a neutral buoyancy design to allow for operational stability. The fuzzy controller uses a vector thrust to maintain altitude. The thrust controller methods have been used in myriad of cases to provide altitude modulation. Efimev [86] published working principles on which a submarine would lean on to maintain operational stability. For the dive stage, ballast tanks fitted to the submarine are filled while the submarine leans upon pre-set trims for ailerons to maintain stability. Submarines for operational safety must quickly flood and empty ballast tanks, at the same time they have a depth control tank that always has access to water. The depth control tank is located at the centre of mass along the length axis. However, to provide stability from wave action to

combat longitudinal forces, the depth control tank is placed at the lowest possible point in the submarine [87]. The outer shell in the case of a submarine must be a circle to limit hoop stresses. A deviation of 0.5% in the dimensions of the outside circular shell can cause the submarine to lose 35% of the hydrostatic load-carrying capacity [87]. The ballast tanks can have multiple opening operated by a control system, and use trim pumps to create a vacuum with water-in pressure set at 20 in of Hg [88].

## 2.8 Remote micro-grids

The new CT-HKT is designed to contribute to baseline power in remote micro-grid system. Micro-grids have been studied to work with different distributed energy resources, thus, making micro-grids technology agnostic [89]–[92]. The design choices depend upon the scale of the project and economic constraints [93]. However, micro-grids lack the inertia of the synchronous generators. Thus, they need a storage system to compensate for inertia during faults. The faults can occur due to imbalances in production, demand, and demand variability [94]. As the micro-grids are focused in a small geographic area as opposed to the vast span of the centralised grids, the demand ramp during peak hours may be less steep. The gradual slope of the demand ramp is favourable to the deployment of renewable energy dependent micro-grids [93]. In the case of remote communities, 100% renewable energy based micro-grids can be developed using HKTs to provide base load power with other case specific renewable energy-based generation sources dealing with the variable energy requirements and an energy storage system for contingencies [95]. Micro-grids have economic benefits as cost of design and building new distribution systems can vary from 24,000 to 62,000

$/km depending upon the terrain and labour costs [96]. Micro-grids also reduce up to 10% transmission losses incurred due to line losses and AC-DC-AC conversion [96].

## 3. Design of the CT-HKT

To achieve research objectives, it is required to design and test a single rotor tethered CT-HKT in a highly energetic river at CHTTC located downstream of the Seven Sisters Generating Station. The design challenges that needed to be addressed in the conceptualized new turbine for successful deployment in a highly energetic riverine system for year-round operation include:

- Turbine system that would be deployable from a shallow riverbank
- A towable turbine support system with ease of deployment
- A turbine with the ability to dive and be operable in the water column

The design of the CT-HKT design requires the formulation of analytical models:

- A *counter torque* model to balance the shaft power produced at a given river velocity and use to show that the CT-HKT can address the maximum rated generator power.
- A *buoyancy* model to predict the turbine position up and down in the water column, and to maintain its position in the free stream. The free stream is set at approximately 30% of the river depth. The ability to dive allows the turbine to avoid any debris present, especially during the snowmelt season.

The CT-HKT is an amalgamation of mechanical and electrical components. The components can be broadly classified as:

- Chassis for CT-HKT
- A suitable generator for operation in submerged conditions

- Control system
- Impeller assembly
- Counter-torque medium

Figure 18 shows the schematic for the CT-HKT to be designed.

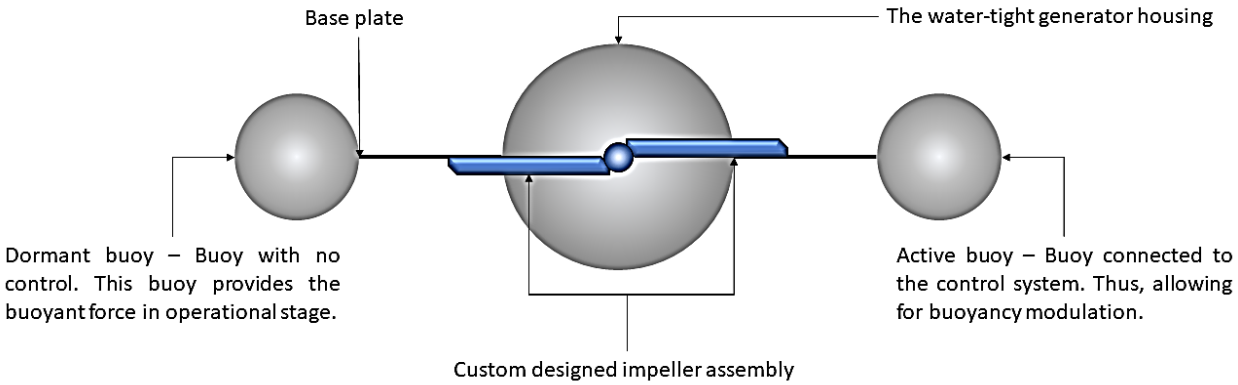


Figure 18: Schematic representation of the CT-HKT.

## 3.1 Design methodology

The iterative process of HKT design can be divided into the following steps.

- Selection of components
- Numerical modelling
- CAD design of field prototype

These steps used to design the CT-HKT are described in the sections below.

## 3.2 Selection of components

Selection of components is a critical part of the design process. Each working component has specific characteristics and specifications. The parameters used to select working components are detailed in Table 6.

Table 6: The qualification parameters for each of the sub-systems involved in the design of the single rotor tethered CT-HKT.

| # | Working components | Primary qualification characteristics | Other qualification characteristics |
|---|---|---|---|
| 1 | Power Generation | Power curves | Rated power and weight |
| 2 | Control System | Linear sensitivity response | Linear response to pressure changes |
| 3 | Control Unit | Volume, Mass | Pressure rating |
| 4 | Chassis | Mass | Structural rigidity |

The component selection involved the electrical generator and fluid gear pumps to design the counter torque system and material selection using aluminium and ABS for the housing.

Two design concepts were considered for power extraction. The motivation leading to the two concepts was to keep the physical footprint of the system to a bare minimum. The qualifying concept was the direct shaft design, where the impeller is coupled to the shaft with a seal.

The second method was to use fluid pumps to transfer energy from impeller to a generator on the surface. Such a design concept would reduce the mass and footprint of the system under water significantly. However, elements through the air-water interaction would render the system inoperable during winters due to ice formation, thus, not be suited for

micro-grids requiring year-round operability. Table 7 lists shortlisted generator candidates for the CT-HKT.

Table 7: Generators considered for the CT-HKT.

| # | Generator Name | Rated Power (kW) | Rated RPM | Rated Torque (N-m) | Marketed Weight (kg) |
|---|---|---|---|---|---|
| 1 | MOOG - Ag-12600-A-1ES | 1.0 | 250 | 48.54 | 9.5 |
| 2 | MOOG -Ag-7350-B-1ES | 1.3 | 600 | 24.41 | 6.6 |
| 3 | MOOG-AG-5250-F-1ES | 1.4 | 650 | 24.95 | 7.5 |
| 4 | Alxion - 190STK2M | 1.1 | 500 | 32 | 13 |
| 5 | Parker- TKA131HLKZB2R1000 | 2.78 | 940 | NA | NA |
| 6 | ICPE -KSO/H230 050 | 2.7 | 630 | 164.4 | 8.3 |

Table 7 also provides the generator specifications. It is important to note that the manufacturers rate the generators at higher output than the design point set at 500 W for the first in-situ porotype. A generator with an output of 500 W at 200 rpm is selected. Generator output design constraint was applied to reduce vibrations. The impeller was designed using CFD and then manufactured within our research group using rapid prototyping 3D printing. 3D printing is economical and advantageous over traditional methods when designing prototypes. Figure 19 shows the CAD model of the impeller and generator assembly.

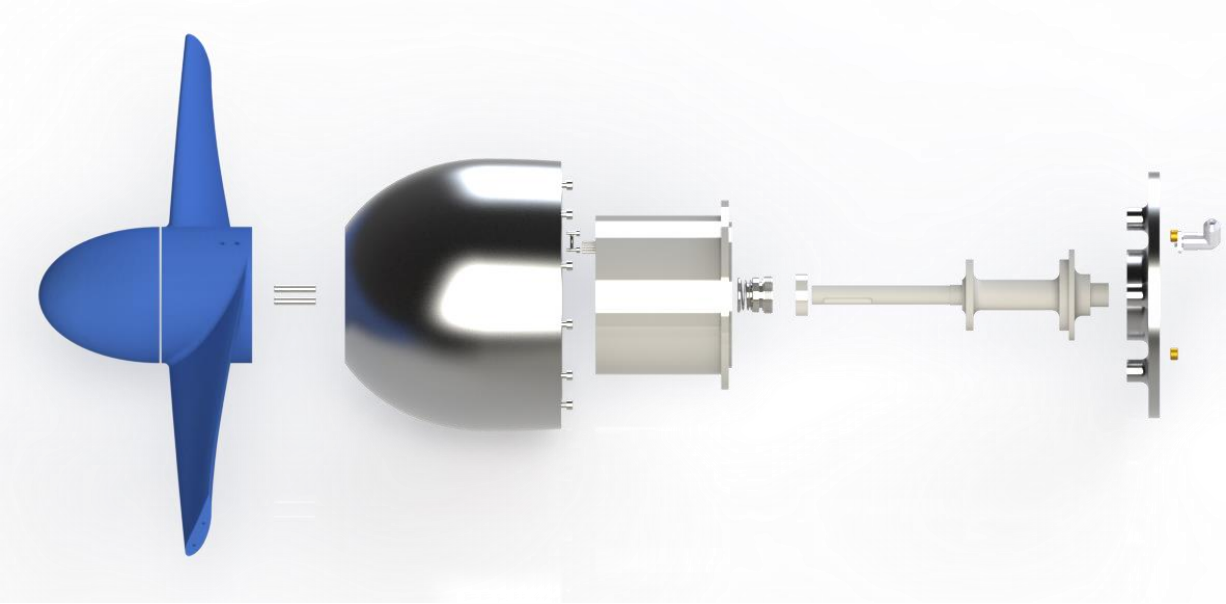

Figure 19: Final generator and impeller assembly. The generator assembly is comprised of a custom designed shaft, the Moog-Ag-12600-A-1ES generator and a custom design watertight housing.

Once the generator is selected, parameters pertaining to torque required to produce the design point power, mass, volume, and RPM of the generator at design point power is then established. Properties of the selected generator are presented in Table 8.

Table 8:The physical and operational specifications of the selected generator, MOOG-Ag-1200-A-1ES.

| **MOOG - Ag-12600-A-1ES** | |
|---|---|
| **Parameter** | **Value** |
| **Rated torque** | 48.54 N-m |
| **Rated RPM** | 250 RPM |
| **Rated output** | 1.0 kW |
| **Mass of generator and housing** | 16.72 kg |
| **The volume of generator and housing** | 5.65 Litres |

The properties of the generator allow for multiple dimensional combinations of the CT-HKT system design. Such combinations are possible because of multiple governing

equations that yield multiple solutions. To reduce the time involved to evaluate each dimensional combination, two numerical models were developed in MATLAB, which are presented in the next sections.

## 3.3 Numerical models

A numerical model was developed to obtain the various dimensions allowing for the stability of the system in transport and operational phases of the turbine's duty cycle. The models considered of static, dynamic and buoyancy equations. The following assumptions were made while modelling the counter-torque system:

- Density of water - 997 kg/$m^3$
- Density of aluminium - 2700 kg/$m^3$
- Density of ABS - 1080 kg/$m^3$
- Acceleration due to gravity - 9.81 m/$s^2$
- Flow-velocity - Constant.
- Density of air - 1.205 kg/$m^3$
- The valves have only two states - Open and close
- The latency between the signal and the opening and closing of valves - Instantaneous.

There are a number of design configurations depending upon the angle of operation from 0º to 45º, generator torque from 0 to 50 N-m, flow velocity 0 to 3 m/s, length of arms, the diameter of each buoy, and the mass of the system. These are set as inputs in the analytical models.

### 3.3.1 Static model

The static model predicts the behaviour of CT-HKT in equilibrium during operation for set values of design and operational parameters. A CT-HKT model was established based on the free body diagram of forces, shown in Figure 20.

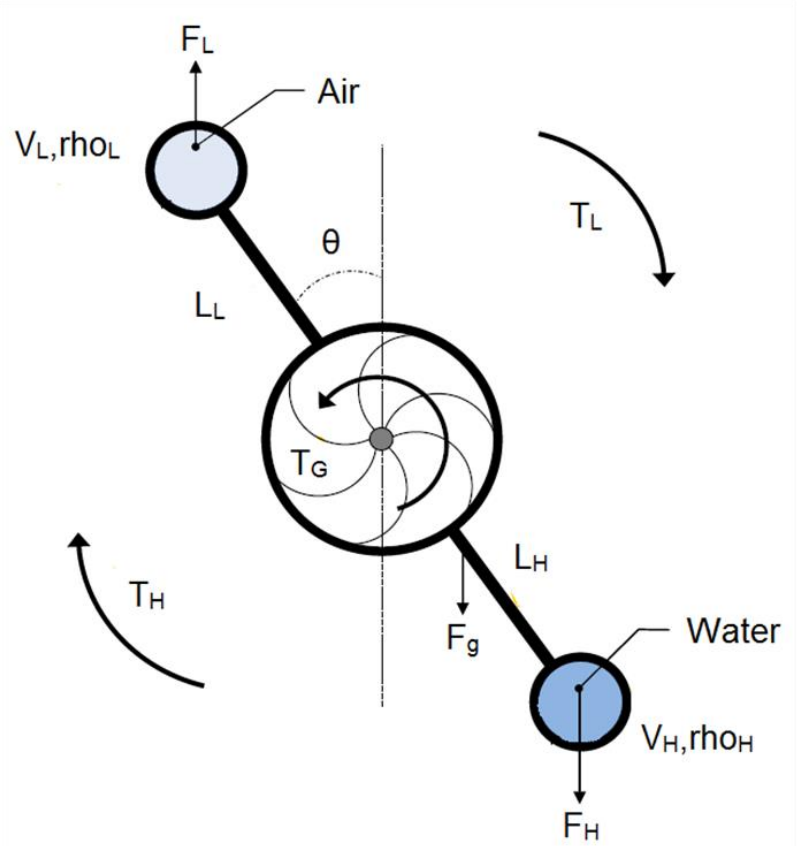


Figure 20: When the CT-HKT is in an operational configuration, the torque are generator torque ($T_G$) and torque due to forces exerted by the buoys at either end of the CT-HKT ($T_L$ and $T_H$). When the net torque produced by the CT-HKT is zero, the CT-HKT will extract maximum available power. $T_L$ is dependent on the volume of the light buoy ($V_L$), density of air (rho$_L$), the angle of inclination (θ), and distance from the center ($L_L$). $T_H$ is dependent on the volume of the heavy buoy ($V_H$), density of water (rho$_H$) the angle of inclination (θ) and distance from the center ($L_H$).

The counter torque provided by the system is set to the cross product of the distance between each buoy and the generator shaft to the net force applied by the buoy assembly. The distance between each buoy and the generator shaft is the same owing to the axis

of symmetry of the turbine. The force exerted by each buoys, $F_{\mathrm{NB}}$, is given by the sum of forces due to the mass of the buoy, $F_B$, mass of the water if present inside the buoy, $\mathrm{F}_W$, and the buoyant force due to the air in the buoy, $B_A$ so that

$$F_{\mathrm{NB}} = F_B + \mathrm{F}_W - B_A \tag{2}$$

where

$$F_B = N\,V \tag{3}$$

Here, N is the number of buoys used to provide the force required, and V is the volume of each buoy, and

$$\mathrm{F}_W = \rho_{\mathrm{w}}\ \mathrm{g}\ \mathrm{V}_{\mathrm{w}} \tag{4}$$

$$B_A = \rho_{\mathrm{w}}\ \mathrm{g}\ \mathrm{V}_{\mathrm{a}} \tag{5}$$

where $\rho_{\mathrm{w}}$ is the density of water, g is the acceleration due to gravity, $\mathrm{V}_{\mathrm{w}}$ is the volume of water in the buoy and $\mathrm{V}_{\mathrm{a}}$ is the volume of air in the buoy. Substitution gives

$$F_{\mathrm{NB}} = [N\,V] + [\rho_{\mathrm{w}}\ \mathrm{g}\ \mathrm{V}_{\mathrm{w}}]\ - [\rho_{\mathrm{w}}\ \mathrm{g}\ \mathrm{V}_{\mathrm{a}}] \tag{6}$$

In the case of a sealed lighter buoy located above the turbine, the force due to water in the buoy is set to zero, and the equations become

$$F_{\mathrm{LB}} = F_B - B_A \tag{7}$$

$$F_{\mathrm{LB}} = [N\,V] - [\rho_{\mathrm{w}}\ \mathrm{g}\ \mathrm{V}_{\mathrm{a}}] \tag{8}$$

While the force due to the heavier buoy below the turbine, $F_{\mathrm{HB}}$,

$$F_{\mathrm{HB}} = F_B + \mathrm{F}_W - B_A \tag{9}$$

$$F_{\mathrm{HB}} = [N\,V] + [\rho_{\mathrm{w}}\ \mathrm{g}\ \mathrm{V}_{\mathrm{w}}] - [\rho_{\mathrm{w}}\ \mathrm{g}\ \mathrm{V}_{\mathrm{a}}] \tag{10}$$

In the design process, for the operation of the turbine, the torque produced by the generator needs to be balanced to maintain system stability. Torque is defined as the product of the force applied and the shortest distance between the axis and the direction of the force. Therefore, the maximum torque available to the system, $T_T$, can be expressed as the sum of torques from light buoy, $T_L$, and heavy buoy, $T_H$, as

$$T_T = T_L + T_H \tag{11}$$

where

$$T_L = F_{LB}\, D\, \sin\theta \tag{12}$$

$$T_H = F_{LH}\, D\, \sin\theta \tag{13}$$

where D is the shortest distance between the torque required to produce shaft power and the force exerted by the buoys, and $\theta$ is the angle between the turbine and the horizontal plane passing through the chassis. The shortest distance, D, is limited by the dimensions of the impeller which must exceed the radius of the impeller and theoretically can have a much larger value. However, a large D will result in a significantly heavy CT-HKT, thereby requiring significantly larger floatation. Figure 21 shows operation angle vs torque produced by the Matlab model.

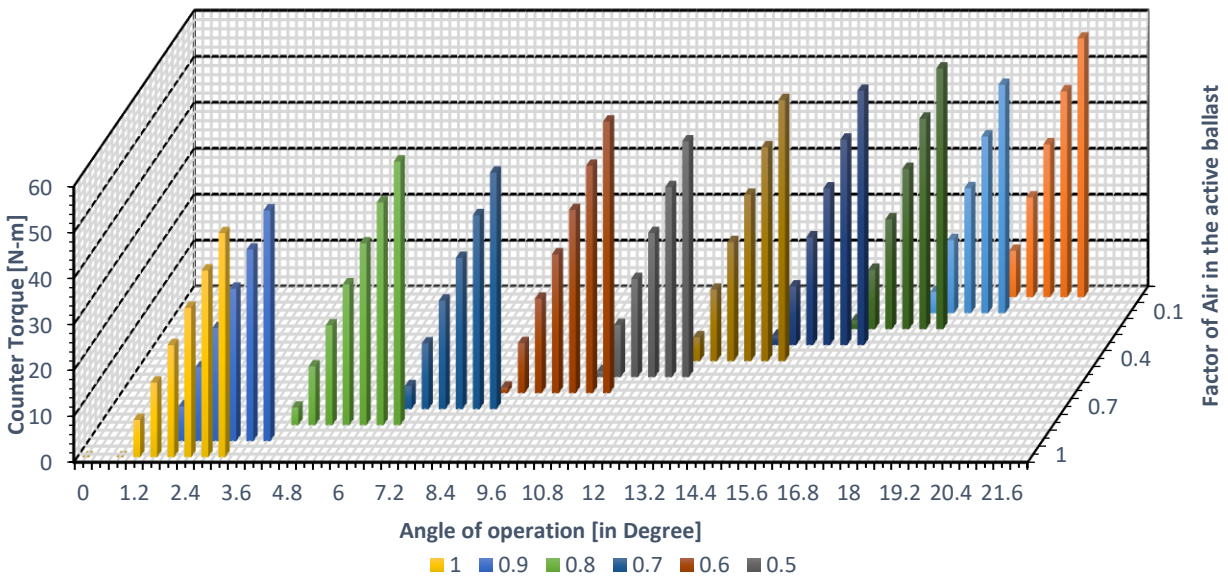


Figure 21: Plot of different torque values available at various operational angles and levels of buoyancy.

To achieve a static counter-torque balance, one of the buoys can be filled with a medium to change the buoyancy. In this case, water is the chosen medium as it is readily available and can be discharged into the surroundings. The introduction of water to lower buoy of the CT-HKT system impacts the centre of gravity and, therefore, affecting the free body configuration of the system. The change in centre of gravity results in the change in axis of rotation of the CT-HKT system, thus changing the forces exerted onto the system. The following equations show how the variation in center of gravity affects the system:

$$T_L = F_{LB}(D + \triangle d)\sin\theta \tag{14}$$

$$T_H = F_{LH}(D - \triangle d)\sin\theta \tag{15}$$

where $\triangle \mathrm{d}$ is the change in the center of gravity towards the heavier buoy. As $\triangle \mathrm{d}$ increases in magnitude further mass is required. Thus, during the sinking or resurfacing process, the center of gravity of the CT-HKT system continuously changes thereby adding to the design challenge. The movement of center of gravity changes the axis of rotation, the static equation in this case is given by

$$\mathrm{T_T} = \mathrm{T_L} + \mathrm{T_H} - T_G \tag{16}$$

where the torque on the shaft due to the generator is given by $T_G$.

The static model with the inputs like acceleration due to gravity, density of water and air, and torque on the shaft due to the generator can give a matrix of solutions with various combinations for the length of arms and volume required to achieve the required counter torque.

### 3.3.2 Buoyancy model

The buoyancy model predicts the behaviour of CT-HKT system when additional mass is added or removed during stages of deployment. The buoyancy model uses the principle of buoyancy. The buoyant force is provided by the presence of the two volumes at either end that displaces liquid heavier than the mass of the system. For the system to work effectively, it is necessary that the lighter upper buoy be able to keep the system buoyant by itself and simultaneously allow the system to move vertically in the water column. $M_{HKT}$ gives the mass of the CT-HKT system, the buoyant force due to the heavier buoy is given by $N_{HB,}$ and buoyant force due to the lighter buoy is given by $N_{LB.}$ For the system to be neutrally buoyant

$$M_{HKT} - (F_{HB} + F_{LB}) = 0 \quad (17)$$

The mass of water required for the system to achieve neutral buoyancy is calculated. Any mass greater than the calculated value would lead to the system exhibiting negative buoyancy, and any value less would contribute to positive buoyancy.

The equation for the system to achieve neutral buoyancy can be expanded as follows

$$M_{HKT} - [(F_{BL} - F_{ML}) + (F_{BH} - F_{MH})] = 0 \quad (18)$$

Here, $F_{HB}$ is the difference between the buoyant force due to the heavier lower buoy and the mass of the buoy. The mass of heavier buoy includes the mass of the water in the operational stage. $F_{LB}$ is the difference between the buoyant force due to the light upper buoy and the dry mass of the buoy. In the case of the heavier buoy, as the mass of water in the buoy increases and the buoyant force available from the buoy will decrease with increasing system mass.

### 3.4 CAD design of field prototype

This section focuses on details of how the CT-HKT system is designed with the integration of its components. The integration of all the functional components was done using Solidworks CAD package. The initial design was undertaken using a numerical model made in excel, which was then migrated to Matlab. The CAD design accommodates the electrical and mechanical components while also addressing loads effecting the CT-HKT.

The operational viability of the CT-HKT system is based on Newton's 3rd law of motion which is achieved by countering the effects of generator torque. The active ballast at one end of the system is provided with the ability to modulate mass to provide counter-torque. The modulation of mass allows for the active ballast side to become negatively buoyant while the ballast provides operational stability. CAD design involved developing individual components for a sub-system assembly which were integrated in the CAD model.

### 3.4.1 Blade design

Once the specifications of the generator unit were fixed, the amount of torque needed to produce design point power is calculated. The Matlab model for the CT-HKT provides the geometric constraints for the dimensions of the impeller.

The focus of the two-bladed impeller design was on performance enhancement and optimization of the lift region. Simulations of four-digit NACA aerofoils were conducted. The NACA four digits signify the camber, position of the maximum camber and thickness using the notation MPXX where

- M is the maximum camber divided by 100,
- P is the position of the maximum camber divided by 10, and
- XX is the thickness divided by 100.

The NACA aerofoil section is created from a camber line, and a thickness distribution

plotted perpendicular to the camber line. The equation for the camber line is split into sections either side of the point of maximum camber position, p. To calculate the position of the final aerofoil envelope, the gradient of the camber line is required. The equations for the locus of the aerofoil are given below.

CAMBER

- For $p = [0 \leq x < p]$

$$y_c = \frac{M}{p^2}(2px - x^2) \tag{19}$$

- For $p = [p \leq x \leq 1]$

$$y_c = \frac{M}{(1-p^2)}(1 - 2p + 2Px - x^2) \tag{20}$$

GRADIENT

- For $p = [0 \leq x < p]$

$$\frac{dy_c}{dx} = \frac{2M}{p^2}(p - x) \tag{21}$$

- For $p = [p \leq x \leq 1]$

$$\frac{dy_c}{dx} = \frac{2M}{(1-p^2)}(p - x) \tag{22}$$

THICKNESS DISTRIBUTION

$$y_t = \frac{T}{0.2}(a_0 x^{0.5} + a_1 + a_2 x^2 + a_3 x^3 + a_4 x^4) \tag{23}$$

where

- $a_0$ = 0.2969,
- $a_1$ = -0.126,
- $a_2$ = -0.3516,
- $a_3$ = 0.2843, and
- $a_4$ = -0.1015 or -0.1036 for a closed trailing edge.

The constants $a_0$ to $a_4$ are for a 20% thick aerofoil. In Equation 25, T/20 adjusts the

constants to the required thickness. At the trailing edge at x = 1, there is a finite thickness of 0.0021 chord width for an aerofoil with 20% thickness. If a closed trailing edge is required, the value of $a_4$ can be adjusted. The value of $y_t$ denotes half thickness and needs to be applied both sides of the camber line.

Using Equations 21 to 25, for a given value of x, it is possible to calculate the camber line position, Yc, the gradient of the camber line, and the cord thickness. The position of the upper and lower surface can then be calculated perpendicular to the camber line using

$$\theta = \text{atan}\left(\frac{dy_c}{dx}\right) \tag{24}$$

where for the upper surface

$$x_u = x_c - y_t \sin(\theta),\ y_u = y_c + y_t \cos(\theta) \tag{25}$$

and for the lower surface

$$x_1 = x_c + y_t \sin(\theta),\ y_1 = y_c - y_t \cos(\theta) \tag{26}$$

The method to determine the shape of the aerofoil is to iterate through equally spaced values of x calculating the upper and lower surface coordinates. While this works, the points are more widely spaced around the leading edge where the curvature is highest, and flat sections can be seen on the plots. To group the points at the ends of the aerofoil sections, cosine spacing is used with uniform increments of β

$$x = \frac{(1-\cos(\beta))}{2} \qquad \text{for } 0 \leq \beta \leq \pi \tag{27}$$

The simulations were done using the Xflr5 shareware program. The Reynolds number for the simulations was set at 200,000 and 500,000. These values were chosen as they correspond to the design point velocity of the CT-HKT. The simulations set the Ncrit number to 4 which models the turbulence effect of the fluid flow field. The set value of 4 corresponds to a dirty wind tunnel [97]. The Mach number was set to 0, to signify a subsonic flow.

The $c_l/c_d$ results of the simulations showed that when Reynolds's number is set at 500,000, the lift to drag ratio increased from 47 for NACA 0006 to 110 for NACA 6412. This trend holds while Reynolds's number is set at 200,000 and is critical while selecting the starting profile for the lift producing region of the blade. The impeller cut section is selected from the analysis done on the aerodynamic properties of the NACA 4-digit profiles. Once the cut-section is set, variables are parametrized in Solidworks.

The parameterized model for the impeller has the following governing variables. The root section and the tip section of the impeller are defined by thickness, angle of attack, and chord length. The length of the impeller was constrained to a maximum of 580 mm. The mesh and analysis for the optimization were done in ANSYS CFX. The mesh is set-up to be fine near the blade region, with the maximum length of the cell set at 1 mm near the impeller. While near the nose of the impeller, the maximum face length was set at 2.5 mm. Ten inflation layers near the impeller were set with the rate of inflation at 1.05. The nose had 10 inflation layers therefore every layer would see the maximum face size increase of 5%. The flow field is divided into two parts, namely, focus and

domain. This is done to reduce the computational resources required to optimize the impeller. The eventual set-up for the impeller had 1.1 million nodes and 3.6 million elements. Table 9 lists the dimensions of the candidate impeller is listed below and Figure 22 shows the mesh used for the optimization of the turbine blade in ANSYS. Once the optimization was achieved, to demonstrate grid independence the candidate points were run at 2.5 million nodes and 8.1 million elements. The simulation was run using the K-epsilon model. The torque and power curve optioned form the CFD, using Ansys CFX simulations are shown in

Figure 23. The final design of the two-bladed optimized rotor is shown in Figure 24.

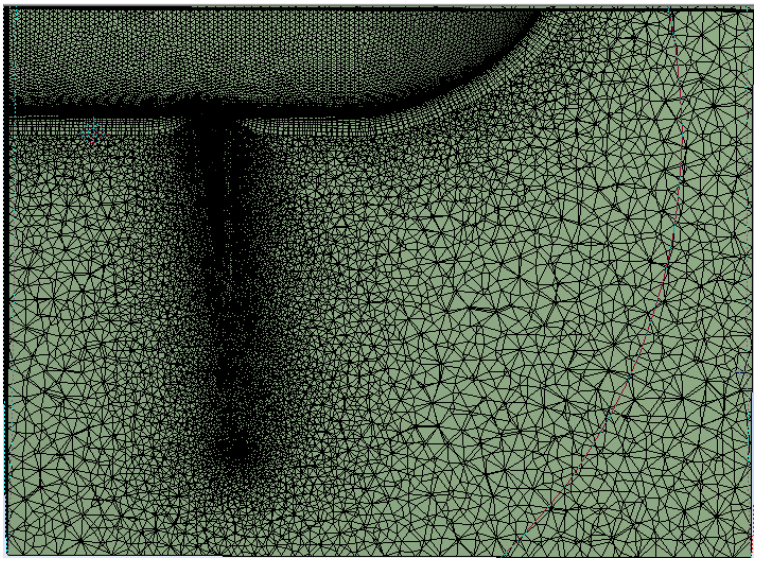

Figure 22: A close-up of the mesh used to optimise the blade geometry.

Table 9: The values of the optimized impeller using ANSYS CFX to be manufactured by rapid prototyping.

| Parameters | Value |
|---|---|
| Average chord length | 99.06 mm |
| Swept area | 0.258 $m^2$ |
| Max nose height | 190.5 mm |
| Average thickness | 20.32 mm |
| Average angle of attack | 22.2º |
| Maximum power | 498.4 W |
| Maximum torque | 25 N-m |

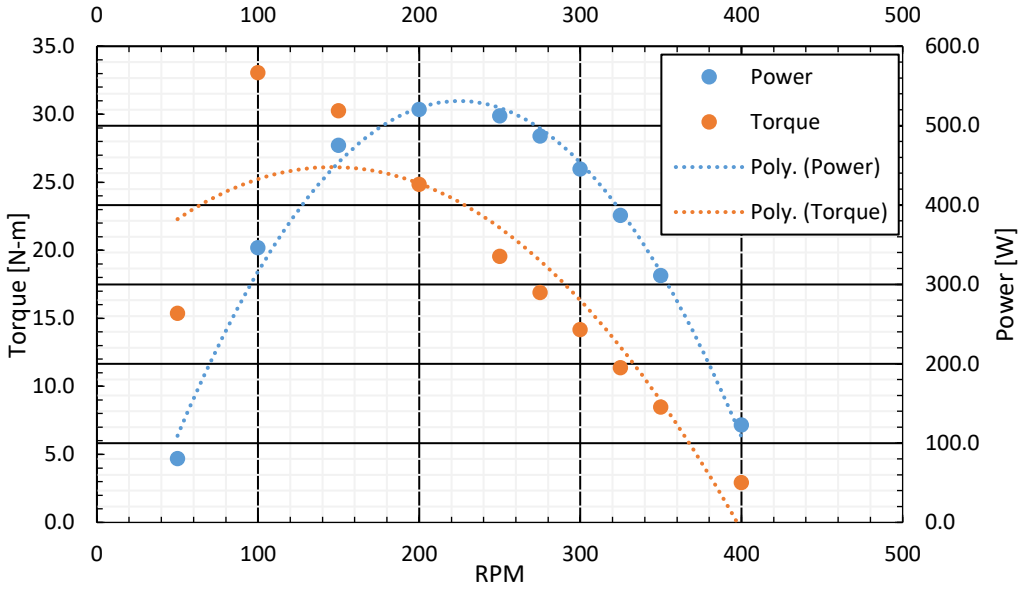


Figure 23: The power and torque vs RPM of the optimised impeller using ANSYS CFX.

The side view of the impeller assembly is shown in Figure 26. The impeller is held under compression using bolts tightened at either ends of the rods running through the impeller. These rods form the spine of the impeller and provide structural integrity to the 3D printed impeller assembly. While the 3D printed geometry forms the fluid dynamic geometry responsible for lift forces to produce torque.

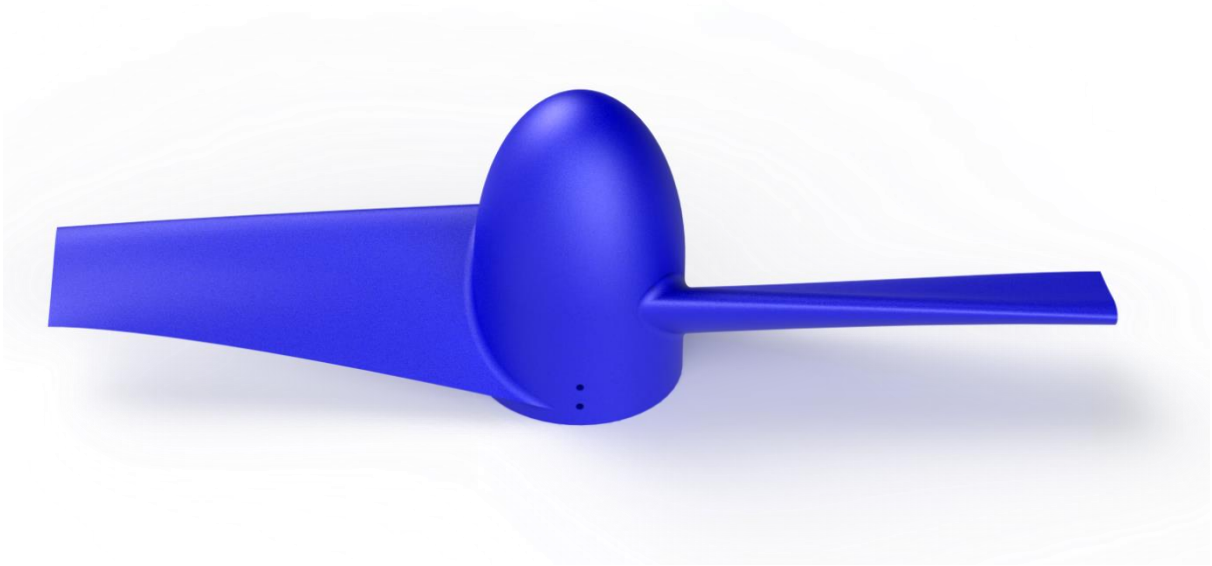

Figure 24: The 3D printed impeller assembly. The impeller is comprised of 3 parts namely hub, blade, and nose cone.

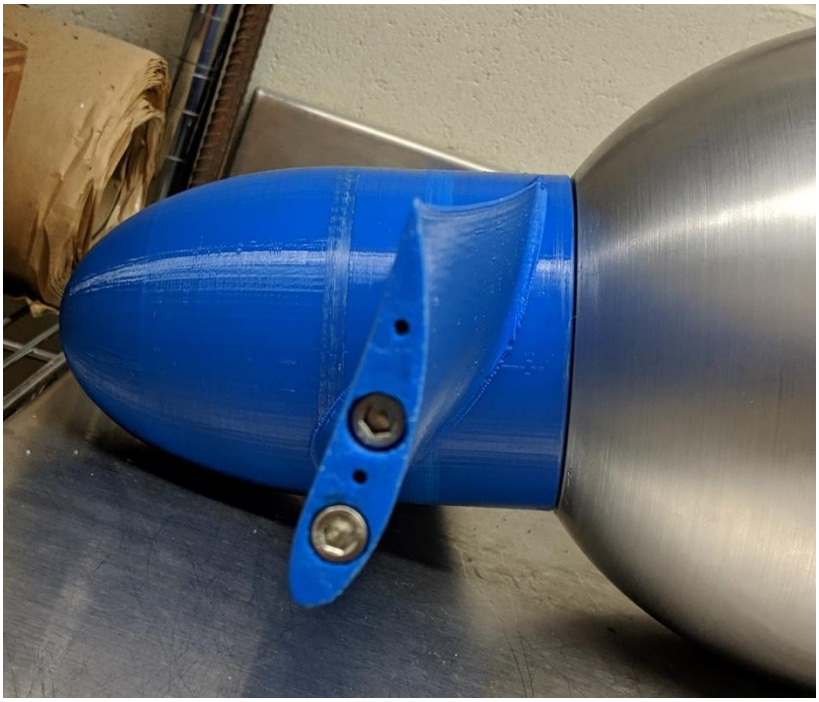

Figure 25: The 3D printed impeller is held under compression by a pair of steel rods running across the impeller. The steel rods provide the structural integrity to the impeller assembly.

### 3.4.2 Floating buoys

The field prototype of the CT-HKT system design finally adopted consists of three buoys, all having the same dimensions to have operational stability during the transportation stage. The dimensional similarity simplified the time required during the manufacturing and assembly of the CT-HKT. In the operational stage, all buoys are maintained at positive buoyancy. The net result of all buoys being buoyant causes the CT-HKT system to stay afloat with the buoyancy of 137 kg. While in the operational stage, the single bottom buoy can fill up with water until the system is negatively buoyant. The negative buoyancy is achieved once the lower buoy is filled with 66.96 L of water. The buoys are designed to:

- provide adequate amount of counter-torque so the system can work at peak efficiency, and
- suggest a buoyant force to support the weight of the CT-HKT system.

The model in Section 3.3 calculated the required volumes required to allow for counter torque to be 0.0097 $m^3$ and for transportation stability to be 0.2946 $m^3$, respectively. The larger volume is selected from the two calculated values. If the lower value were to be selected, the system would be negatively buoyant and would not be able to perform either of the tasks. The selection of the larger volume does not hinder the counter-torque ability at the operation point as it is based on Newton's third law and increases the available maximum counter-torque. The buoyancy needed for the system to work means the counter-torque capabilities of the system were 30.3 times more than the maximum operational counter-torque requirements. Although the CT-HKT system has

counter-torque abilities for a much larger rated generator, the buoyancy system is the limiting factor with an operational band of $\pm$ 1.5 L from 66.96 L. The design point power for the generator was established but the generator is rated for a maximum of 1.0 kW. If the CT-HKT experiences higher than design flow velocity the generator would be able to produce more than design power due to higher counter torque ability after an impeller re-design.

The material used to manufacture the buoy assembly has the following characteristics:

- Inexpensive and readily available
- Ability to withstand the pressure of the water column
- No environmental impact

Water and air are chosen as the medium to change the buoyancy of the system. Water is available from the riverine environment, whereas air is delivered using a compressed airline from the boat.

Once the volume of the buoys is now determined, it needs to be moulded to a shape. For the operability of the CT-HKT, the volume enclosed by the buoys does not need to provide any lift. The following shapes were considered for this research.

The CT-HKT system was initially designed using the GNVR shape, as discussed in Chapter 2 but was prototyped using a cylindrical shape. The analysis of GNVR design showed for the CT-HKT to be operational, the GNVR shaped buoys would have a

diameter of 304.8 mm on either side. Figure 17 shows the relationship between diameter and maximum length—with a diameter of 304.8 mm the maximum length of the buoys would be 929.64 mm. A preliminary design for the prototype of CT-HKT was developed using the GNVR profile, used only aluminium, and required $30,000 for manufacturing. The prohibitive cost of the prototype shown in Figure 26 led us to abandon that design and search for a more economical alternative.

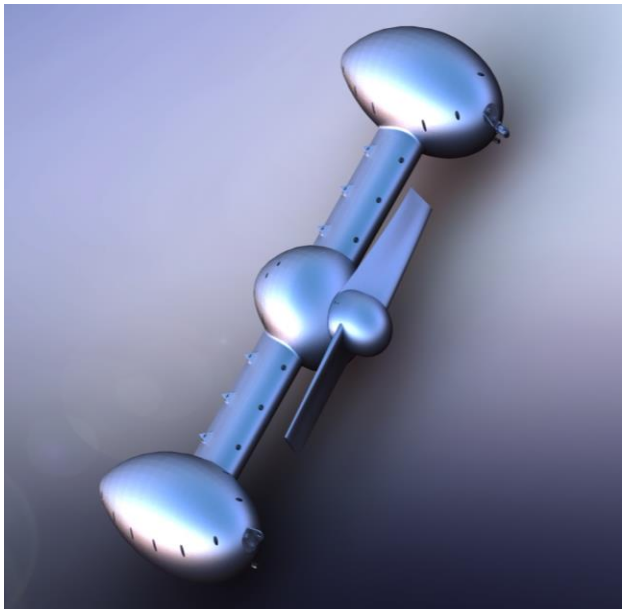

Figure 26: CAD model of the design comprised of GNVR shaped buoys. This all aluminum design was abandoned due to the cost quoted to manufacture the CT-HKT system.

It was decided to use cylindrical shapes for the buoys, as shown in Figure 27. The ballasts were made from Size 10 schedule 40 PVC pipes with pipe covers fused using epoxy-based PVC cement. The advantage of using the Size 10 schedule 40 PVC pipes was that no machining effort was needed which meant shorter lead times. The routing of the control cord and power cable was now done externally. To ensure the power chord was waterproof, the connection points were minimised. The only remaining connection point was joined, and heat shrunk. To ensure there was no slack on the

lines, they were routed in a pre-determined way and pinned to the support structure.

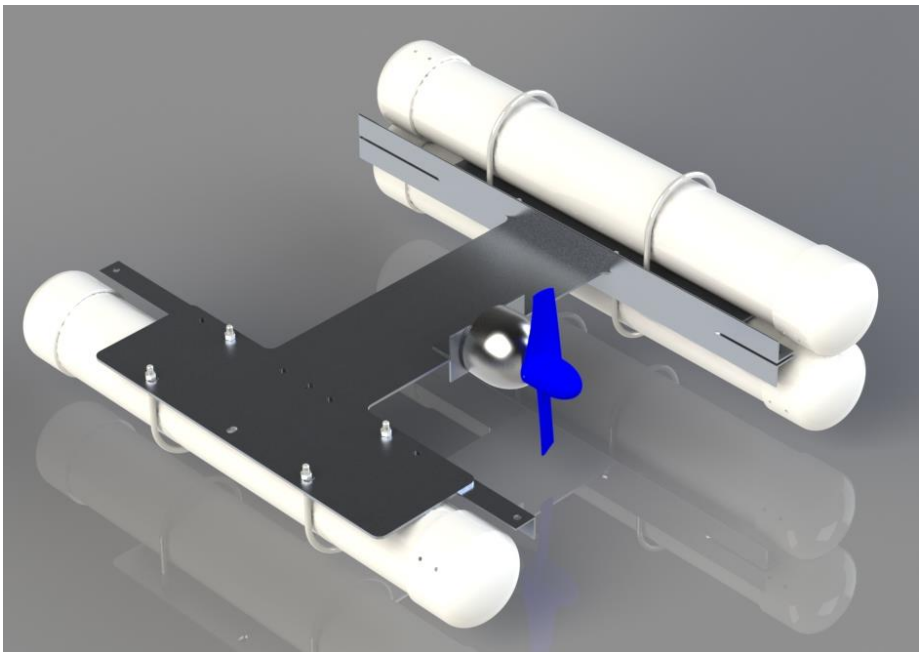

Figure 27: CAD for the single rotor tethered CT-HKT to be tested at the CHTTC.

### 3.4.3 Generator and electronics

The force of the flow acting on the impeller is converted to electrical energy using a generator. The impeller assembly rotates the shaft causing a variation in electrical flux thereby producing current. The CT-HKT system presented in this research is gearless. Doing away with gearbox reduced mechanical losses and points of failure. Losses in the power generation sub-system occur due to the presence of friction between rotor and stator, bearings, contact brushes, and resistance of the copper wire present in the winding.

The prototype CT-HKT is designed around the following constrained:

- The designed counter torque system should not interfere with the impeller

assembly.

- The torque applied to the generator should be counteracted by the CT-HKT system.
- The counter torque available from the CT-HKT system should be variable to allow for operation at a range of velocities.
- The floatation system should be able to support the weight of the system.

### 3.4.4 Support structure

The operational components of the turbine were fastened to a single 19.05 mm thick aluminium plate, as shown in Figure 28. The plate was selected with the consideration that it should not yield past the point where the aluminium plate would permanently deform due to instantaneous stresses applied during operation and transportation stages. The shear strength of an aluminium plate is 138 N/mm. A maximum force of 2001.24 N would be encountered if the CT-HKT was to flip over either underwater or otherwise. Such a force is still below the value of 2628.9 N that a 19.05 mm aluminium plate can withstand before deforming. However, the system could still produce much higher instantaneous impact forces while being towed behind the boat, but such a scenario would be improbable.

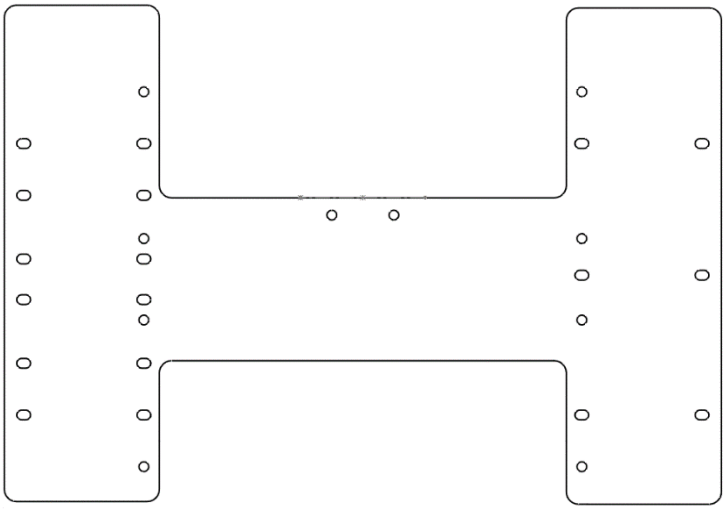

Figure 28: Drawing for the base plate used in the field prototype of the CT-HKT. The Slots were cut on the base plate to account for the manufacturing defects in the U-bolts. While aluminum angles were attached using bolts.

The ballasts were fastened in place using 3 size 10 U-blots each. 12.7 mm thick and 1524-mm long aluminium angles were used to install mooring points, whereas the generator unit was mounted with a 254 mm long aluminium angle. Figure 28 shows the CT-HKT aluminium plate depicting the slots cut on the plate for U-bolts to be attached. The slots for U-bolts were preferred over holes to cater for dimensional tolerances due to the manufacturing process used to manufacture U-Bolts.

### 3.4.5 Control system

The control system is required for two functionalities. Firstly, to allow filling of water in active ballast in order to sink the CT-HKT and secondly, to raise CT-HKT in the water column by expelling water.

The control unit for allowing in water utilises a vacuum pump which produces a

maximum vacuum of -30 in of Hg and is connected to a 5-micron water air separator. The separator is then connected to a valve setup, as shown in Figure 29. The valve setup has a safety switch to normalise the pressure in case of an emergency. The next valve is the vacuum valve attached to a 4-way tee. The 4-way tee has a 2-way pressure gauge connected to one side, the second side has a control chord going to the CT-HKT, and the third side has the compressed air inlet. The compressed air inlet is connected to a compressor which is manually operated through a 1/8" air fill valve. The compressed air inlet connected to the 4-way tee has a safety valve and a standard valve attached inline. The piping on the control unit has a threading of ¼" NPT and is sealed using the Teflon taping.

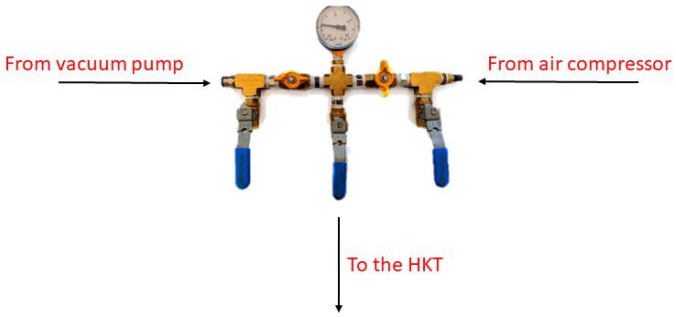


Figure 29: Control system assembled using short pipes, valves, and two-way pressure gauge. The vacuum pump side had an air-water separator attached to prevent damage to the vacuum pump.

The CT-HKT active ballast has two threaded one-way valves. The valve set to take in water is set to open at a pressure of -10 in of Hg and is placed at the top of the active ballast. While at the bottom of the active ballast, the one-way valve to expel water is set to operate at 25 PSI. The land control section is connected via a clear tubing, called control chord. -10 in of Hg was set as the control pressure for a control dive of the CT-

HKT. Pressures lower than -10 in of Hg would allow for the CT-HKT to dive faster; however, in an emergency an evasive measure would be difficult.

**Fabrication** process involved the use of conventional material-removal methods, waterjet, and rapid prototyping to create the parts in the assembly of the CT-HKT system. The generator shaft and casing were fabricated using conventional material removal methods. Such methods have an accuracy of 0.01 mm. The accuracy level is important to produce a non-slip shaft and interference fit and watertight geometry in case of the generator housing. Since the chassis of the HKT is made of a 2-dimensional structure, the geometry is cut from a 2.43 m by 1.21 m aluminium plate using waterjet. The ballasts were cut from a single 5.48 m size 10sch 40 pipe. Similarly, the aluminium angle was cut from a single long angle aluminium angle bar. The appropriately dimensioned aluminium angle was cut on the waterjet to get internal geometries.

**Assembly** of the parts was done in two stages. First, parts like the ballast pipe were fused to the end caps using ABS cement. The process was done in the presence of fume hood and involved making a tiny air bleed hole in the overlap region of the pipe and the end cap. The bleed hole was drilled to allow the air to bleed out of the ballast when the end caps were attached in the desired position. The ballasts were allowed to set for 24 hours for ABS cement to cure. Once the ballasts were set, a leak test using soap water was done on the near the side where the bleed hole was created. Second, the generator sub-assembly is put together using bolts and O-rings. The backplate of the generator housing has an opening to connect the power outlet of the generator to

the power cable running to the shore. The opening is sealed with O-rings and epoxy to maintain the watertight nature of the generator housing. The font of the generator has ceramic bearing to ensure a watertight seal and to avoid rusting. The generator is filled with oil to maintain the pressure equilibrium while operating underwater. Once all the individual components have their sub-assemblies completed, the parts are fastened to the specially cut aluminium plate. The exploded view of the single rotor tethered CT-HKT system is shown in Figure 31.

Figure 30 fitted onto a trailer for easy deployment at the CHTTC. The exploded view of the single rotor tethered CT-HKT system is shown in Figure 31.

Figure 30: CT-HKT mounted onto a zodiac boat trailer for easy deployment at the CHTTC.

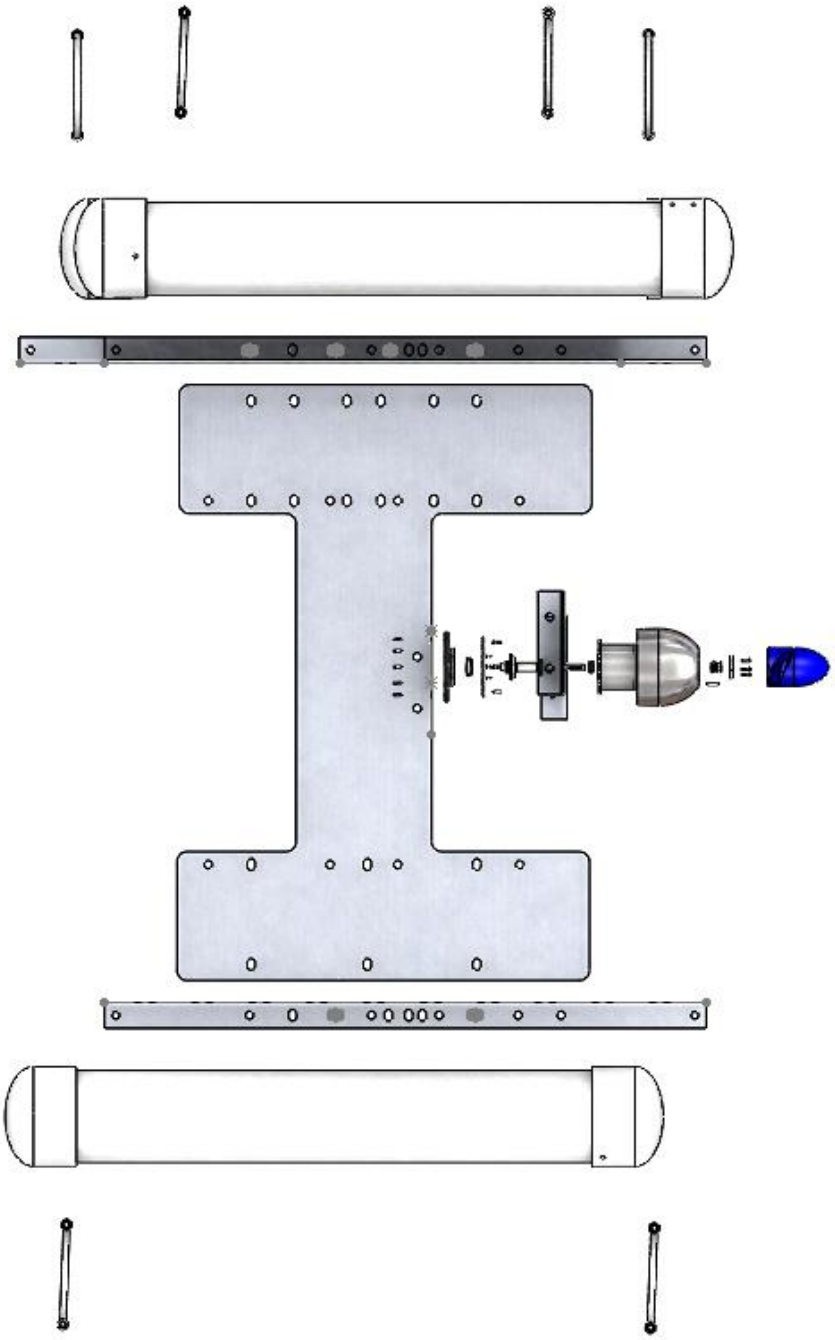

Figure 31: Exploded view of the all the components comprised in the field prototype of the single rotor tethered CT-HKT system.

## 4. CFD set-up and optimization

To demonstrate the operability of CT-HKTs in lower flow conditions, CFD optimization was performed. CFD simulations were first undertaken to replicate the results obtained from a previous scale model turbine tested in a water tunnel. The aim was to validate the accuracy of the CFD model ability to predict the power curve of the CT-HKT. Then, the validated CFD model was scaled-up to simulate the performance of seasonal add-on components to the CT-HKT system to design a system that can operate effectively in micro-grids in low flow winter conditions. Extending the rotor blades is also investigated as a way to address low flow winter conditions.

The CFD model was developed using the finite volume CFD package, ANSYS CFX. The body of the CT-HKT was not considered in the CFD study, as the CT-HKT model would adversely impact the resolution of smaller add-on components, the effect of which is being evaluated. If the CT-HKT body were to be included, the number of nodes would increase by an order of magnitude or the resolution of finite element mesh would have to be decreased, resulting in not accurately capturing the effects of smaller seasonal add-on components. The size of finite element mesh for CFD analysis was based on the smallest component. The smallest mesh size was $4x10^{-4}$ m for shroud optimization, while for the winglet optimization the smallest mesh size was recorded at $1x10^{-4}$ m. The maximum node count was 9 million.

The mesh model, shown in Figure 32, was validated against pre-existing experimental data before starting optimization routine for the seasonal add-on components. To verify

the validity of the CFD model, the following salient aspects from Shahsavarifard et al.'s [62] experiment performed in the water tunnel at the University of Manitoba were simulated. The conditions were:

- Velocity boundary conditions - 1.1 m/s, 0.9 m/s and 0.7 m/s
- Flow field – incompressible water at 25$^{o}$C
- Maximum turbulence measured in water tunnel – 5% at maximum velocity
- Rotor dimensions – Diameter 19.8 cm, Number of blades – 3, length of blade – 7.9 cm, hub diameter meter 3.9 cm and 0.3 cm rounded blade tip to reduce vortices coming off the rotor
- Shrouds
    - Diffuser only
    - Nozzle at the inlet with diffuser at the outlet

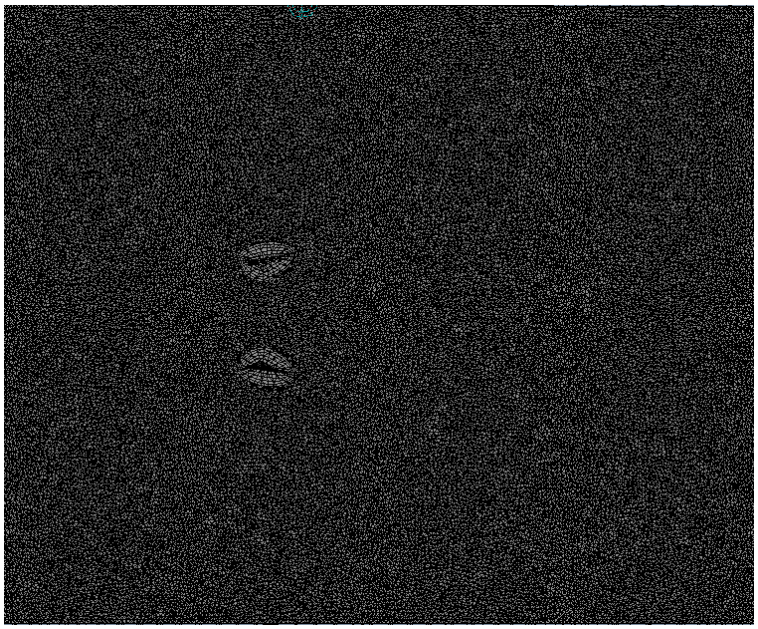

Figure 32: The mesh that is validated against the experimental data from the experiment conducted by Shahsavarifard et al at the University of Manitoba. Once the mesh is successfully validated it is scaled to optimise the shrouds and wingtips.

The dimensions and CAD models of the shrouds and blade are shown in Figure 33 and Figure 34, respectively. The deviation from simulation and the experimental data is given in Table 10.

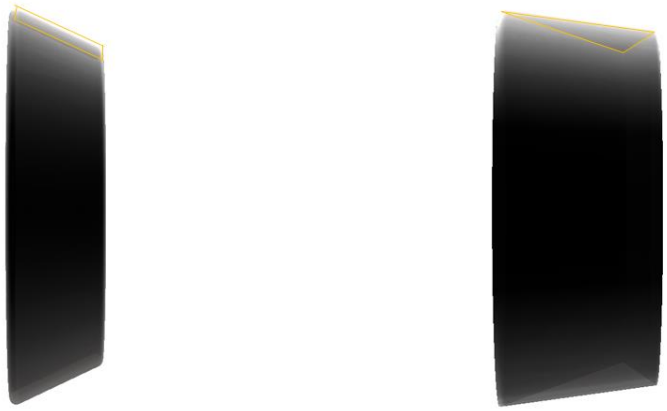

Figure 33: The CAD designs used develop an experimentally validated mesh for CFD optimization for the other add-on components.

Figure 34: CAD model of the blade used in experiments conducted in the water tunnel by Shahsavarifard et al. Blade was modelled to the nearest millimetre so as to reduce errors in the validation study

Table 10: Deviation from the maximum observed velocity during the experiment conducted by M. Shahsavarifard et al. when compared with CFD results.

| Velocity (m/s) | K-Omega | | K-Epsilon | |
|---|---|---|---|---|
| | Shroud | Diffuser | Shroud | Diffuser |
| **1.1** | 0.13 % | 24.20 % | 5.61 % | 28.72 % |
| **0.9** | 3.75 % | 29.47 % | 7.13 % | 33.27 % |
| **0.7** | 6.01 % | 33.50 % | 12.18 % | 36.69 % |

Table 10 establishes that the k-omega model performs better than the k-epsilon model for near-wall calculations. The table also shows that at lower velocities the deviation from the experimental data varies over 20% in case of diffuser style shroud, which is unacceptable.

The original experimental setup was verified at lower velocities. During the experiment it was observed that the blade experienced up to a 20º bending. The blade bending was incorporated in the CFD model. The updated CFD results shown in

Table 11 now are acceptable. The validated model was then used for optimization simulations.

Table 11: The table showing deviation from the maximum observed velocity during the experiment conducted by M. Shahsavarifard et al. when compared against CFD results with deflection modelled into the set-up.

| Velocity (m/s) | K-Omega | | K-Epsilon | |
|---|---|---|---|---|
| | Shroud | Diffuser | Shroud | Diffuser |
| 1.1 | 0.13 % | 10.54 % | 7.84 % | 35.71 % |
| 0.9 | 3.75 % | 19.01 % | 6.81 % | 18.56 % |
| 0.7 | 6.01 % | 0.21 % | 15.78 % | 36.69 % |

The optimization method for the add-on components is based on sampling and sorting. It supports multiple objectives and constraints, as well as all types of input parameters.

This method was used to generate 100 initial design points out of which 3 candidate points was shortlisted. The 3 shortlisted points are taken as the dimensional boundary condition for the next phase. In the next phase, 1000 design points spanning the boundary conditions of the 3 candidate design points are evaluated. From these 1000 design points, 3 final candidates were shortlisted. Optimization was undertaken for the three components - shrouds and winglets.

## 4.1 Shroud

A parametric shroud designs were developed using CAD and was optimised through sampling and sorting method. To arrive at the optimised design for single stage shroud for the CT-HKT the following process was adopted:

### 4.1.1 Diffuser shroud

The diffuser only shroud design of Shahsavarifard et al was taken as the starting point and optimised using a sample and sort method. The data points obtained as part of optimization process provided an insight into how each parameter affected the performance of the diffuser only shroud. The CAD design with various parameters is shown in Figure 35. The iterative parameters for the shroud are given in Table 12 along with the initial boundary conditions. The final 3 candidate after optimization are shown in Table 13.

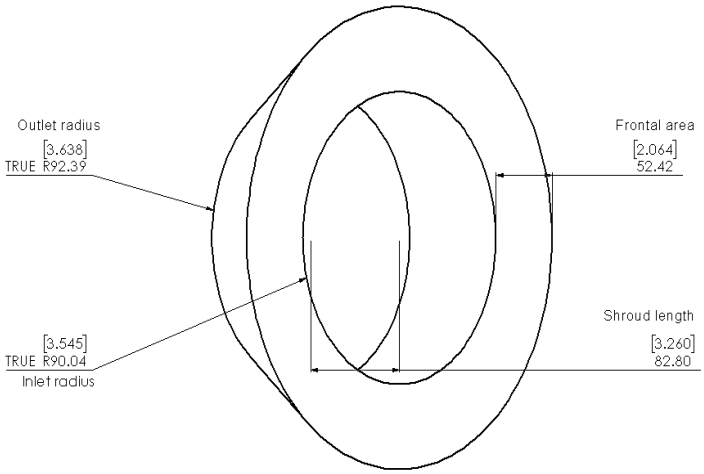


Figure 35: CAD drawing of the Diffuser only shroud.

Table 12: Boundary conditions set for optimizing diffuser only shroud.

| **Parameter** | **Min** | **Max** |
|---|---|---|
| Flow field velocity | 2.0 m/s | |
| Shroud Length | 50.8 mm | 101.6 mm |
| Front depth | 12.5 mm | 63.5 mm |
| Inlet radius | 88.9 mm | 114.3 mm |
| Outlet radius | 88.9 mm | 152.4 mm |

Table 13: Dimensions for the top 3 candidate's diffuser only shrouds with the maximum observed velocity.

| **S.no** | **Outlet radius (mm)** | **Shroud length (mm)** | **Frontal depth (mm)** | **Inlet radius (mm)** | **Accelerated velocity (mm)** | **Percentage increase in velocity (mm)** |
|---|---|---|---|---|---|---|
| 1 | 91.44 | 97.79 | 55.88 | 97.79 | 2.78 | 39 |
| 2 | 92.34 | 83.63 | 55.25 | 96.51 | 2.74 | 37 |
| 3 | 91.73 | 87.79 | 54.00 | 95.66 | 2.74 | 37 |

Figure 36 shows there exists a correlation between increase in frontal area and increase in velocity of the flow field. The graph shows 103 data points out of the 1,106 data points available.

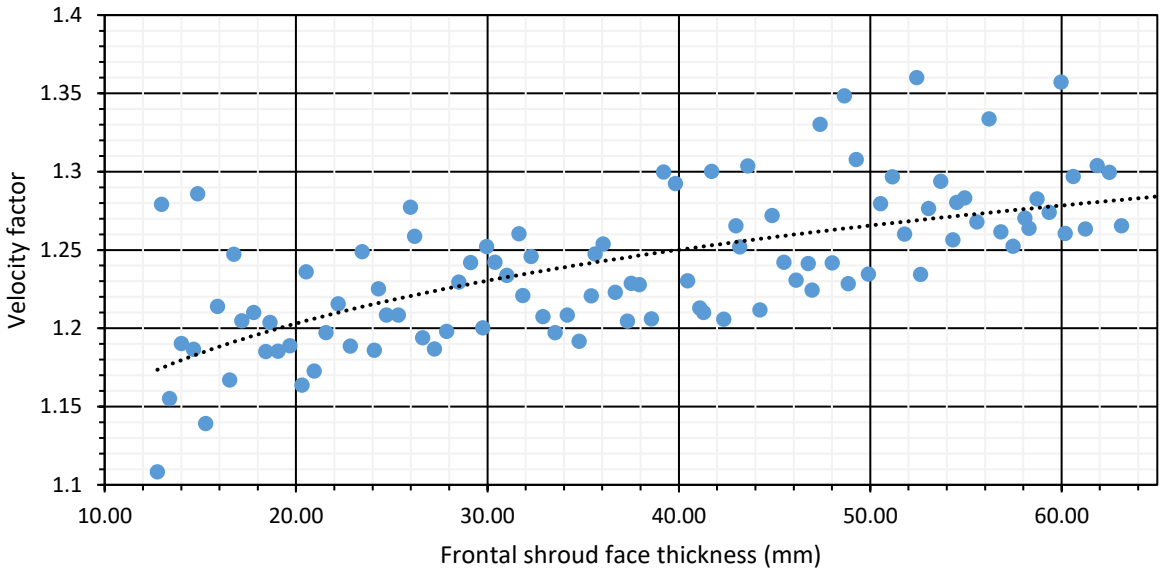


Figure 36: A plot between frontal area of shroud and velocity factor.

The trend line shows the velocity factor increases by 0.08 from 1.17x to 1.25x when the frontal thickness increases by 28 mm from 12 mm to 40 mm. However, for the next 28 mm increase in the frontal thickness the velocity factor goes up by 0.03. The trend line representing the relation between frontal thickness and velocity factor can be observed to plateau past 60 mm. Figure 37 shows the pressure gradient in the horizontal plane and the velocity gradient in the vertical plane around the shroud. Figure 37 shows the pressure barrier forcing more fluid to flow through the shroud. However, as the frontal area increases past 60 mm, the pressure barrier constricts the flow through the shroud. This explains the plateauing observed in Figure 36. Another key observation from Figure 37 is the presence of a higher-pressure region where the flow

through the shroud re-attaches with the rest of the flow field. Moving this region further away from the shroud would increase the strength of the low-pressure region inside the shroud, thus allowing for the higher values of velocity acceleration.

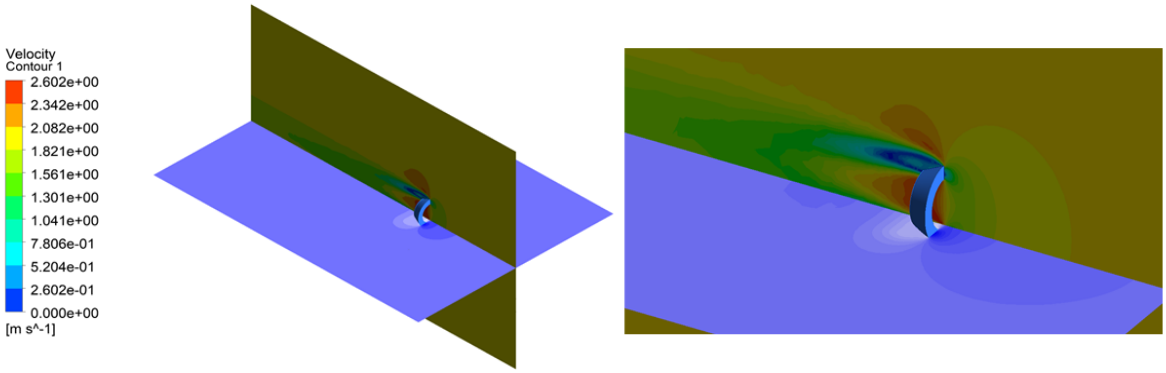


Figure 37: The pressure (horizontal plane) and velocity gradient (vertical plane) recorded for the optimal diffuser only condition. The low-pressure region inside the shroud can be seen pulling the flow thru the shroud.

According to the sensitivity analysis on the data, the two dominating factors for the performance of the shroud are the dimensions of the inlet and the outlet. This is consistent with the theory of continuity. However, according to the theory of continuity maximum velocity that the optimized diffuser only shroud can produce is 2.28 m/s, which correspond to the 14.3 % increase in the flow field. However, a 39.4% increase has been observed. The variation can be explained based on the following as sensitivity analysis shown in Figure 38:

- effect of shroud length, and
- frontal area.

The change in the inlet area, outlet area of the shroud and the maximum velocity are presented in Figure 39.

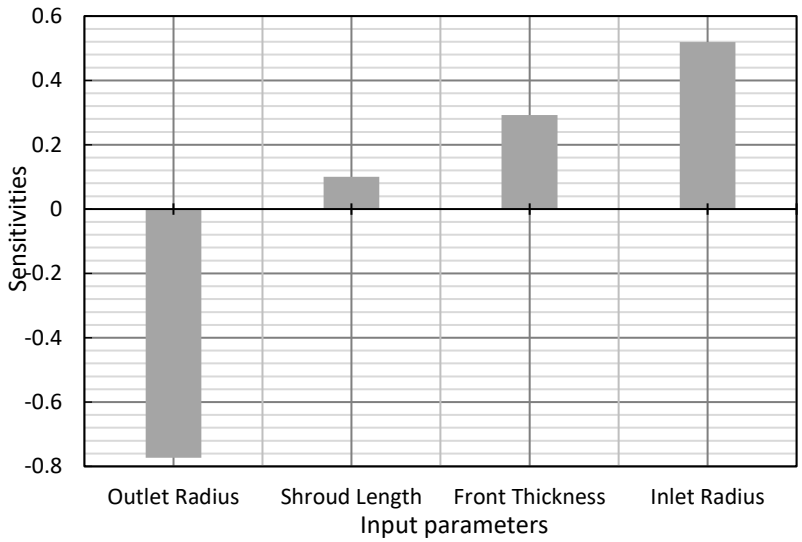


Figure 38: Sensitivity analysis for the range of effect of each parameter on maximum velocity observed inside the diffuser only shroud.

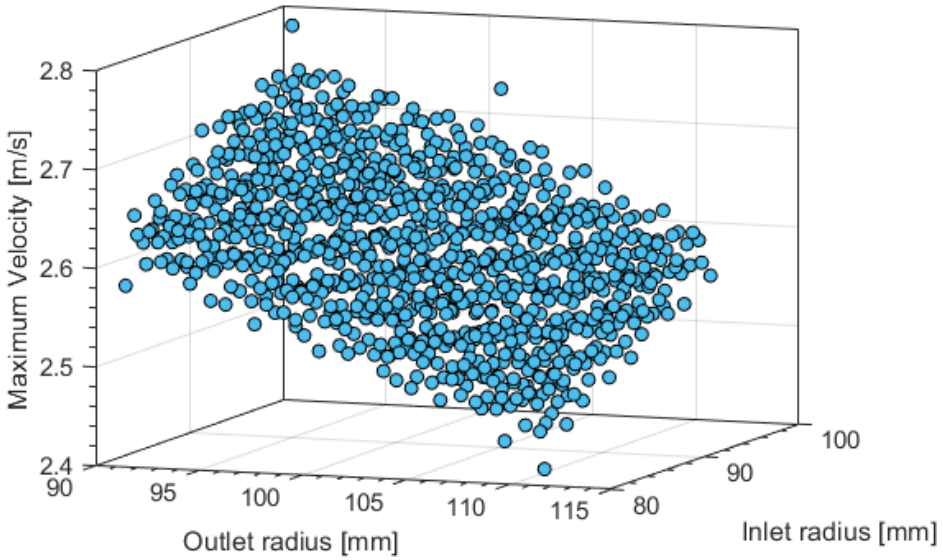


Figure 39: The relation between the inlet radius, outlet radius and velocity. The velocity shows a linear trend concerning the above mention radii with an exception at either end of the chart.

The velocity increase observed as a ratio of Inlet radius and outlet radii shows a linear trend. However, at the extremes the recorded velocity shows a step change. The higher velocity is observed to be in part due to the pressure walls at the inlet being at the optimum strength and the low-pressure region being more extreme. While, during the lower velocity runs, the low-pressure region was minimal whereas pressure walls at the inlet were constricting the flow thru the shroud.

### 4.1.2 Nozzle and diffuser shroud

The shroud for CT-HKT consists of nozzle and diffuser, which evolved from the nozzle and diffuser shroud design by Shahsavarifard et al. The CAD design with various parameters has been labelled in Figure 40.

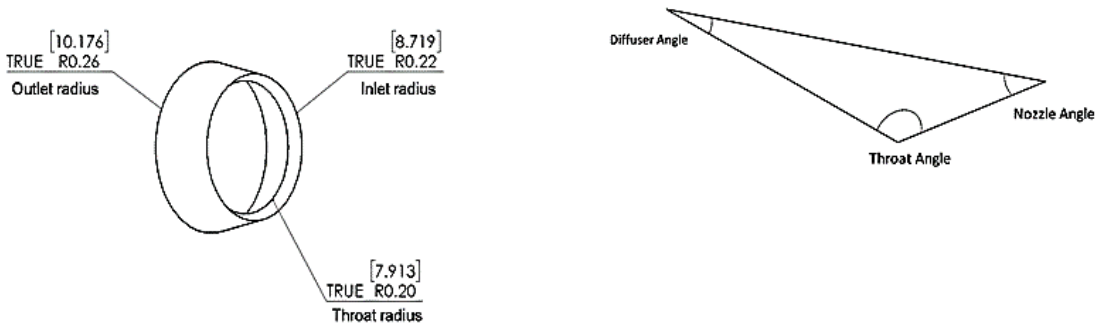


Figure 40: CAD drawing and the cut-section for the nozzle and diffuser shroud.

The iterative parameters for the nozzle and diffuser shroud of the CT-HKT along with the initial boundary conditions are given in Table 14.

The candidate points between the boundary conditions are being optimized to achieve the maximum flow-field velocity. This is measured as the throat plane. The throat plane

region must accommodate the blade while minimising the effect of the wake from the nozzle. The final 3 candidate points on the conclusion of optimization are given in Table 15..

Table 14: Boundary conditions set for optimizing nozzle and diffuser shroud.

| Parameter | Min | Max |
|---|---|---|
| Flow field velocity | 1.0 m/s | |
| Nozzle angle | 25º | 35º |
| Nozzle length | 35 mm | 55 mm |
| Diffuser angle | 20º | 30º |
| Diffuser length | 130 mm | 160 mm |

Table 15: Dimensions for the 3-candidate nozzle and diffuser shrouds with the maximum observed velocity.

| S.no | Nozzle angle (Degree) | Nozzle length (mm) | Diffuser angle (Degree) | Diffuser length (mm) | Accelerated velocity (mm) | Percentage increase in velocity |
|---|---|---|---|---|---|---|
| 1 | 25 | 43.88 | 157.91 | 20 | 1.46 | 46.22 |
| 2 | 25.25 | 46.88 | 148.90 | 20.08 | 1.44 | 44.52 |
| 3 | 25.05 | 47.51 | 153.34 | 20.40 | 1.44 | 44.36 |

Figure 41 depicts sensitivity of various contributing parameters to the maximum velocity in a nozzle and diffuser shroud. As can be observed the dominating parameter is the nozzle angle for the optimum mass flow rate thru the nozzle and diffuser shroud. In theory, higher nozzle angle should allow for a higher fluid flow rate through the shroud. However, the CFD data shows that higher nozzle angle causes the flow field to generate recirculation regions because of the sudden change in the angle of the shroud at the throat region. As these recirculation regions increase in size, the fluid flow rate through the shroud reduces. The diffuser length and angle help in reducing the formation of recirculation regions thereby conditioning the flow field by moving the low-pressure

region further down-stream. As the low-pressure region moves downstream it allows for the increased fluid flow rate through the shroud thus increasing the available power.

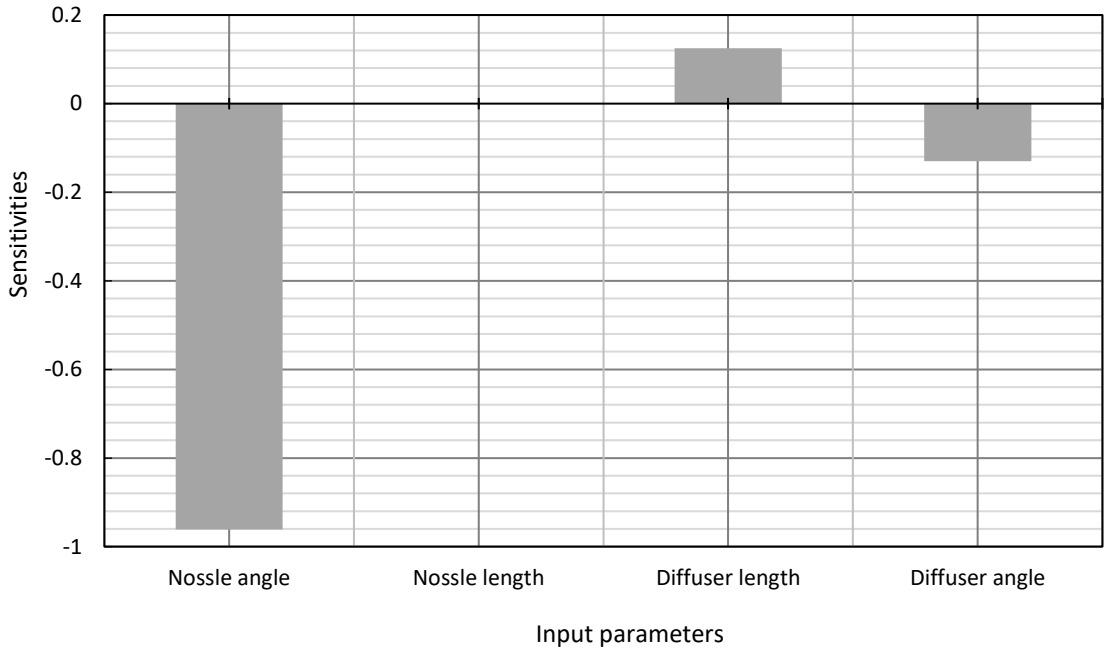


Figure 41: Sensitivity analysis showing the effects of each parameter on the maximum velocity observed at the nozzle and diffuser shroud. Key take way is the how dominant the nozzle angle effects are.

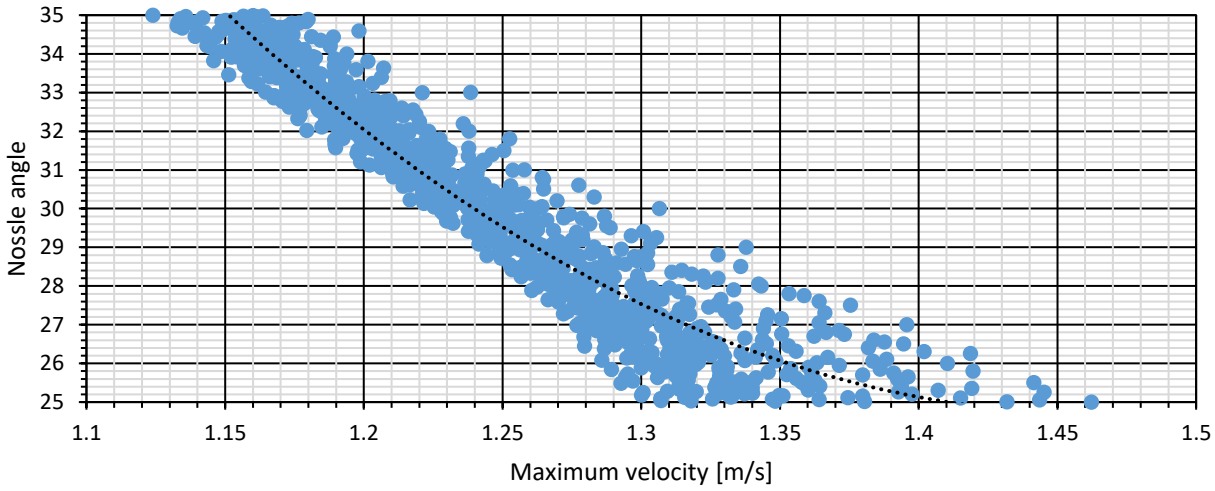


Figure 42: Plot presenting the spreading of the maximum recorded velocity in each iterative run of the simulation.

However, beyond a point, the flow-field starts to detach. This is due to the pressure inside the shroud, falling below the external flow field pressure.

The sensitivity analysis shows that in the given parameters, the length of the nozzle does not affect the shroud performance. Figure 42 shows the nozzle angle of 25º can produce velocities ranging from 1.30 m/s to 1.46 m/s due to diffuser geometry. Whereas the nozzle angle of 35º results in velocities ranging from 1.12 m/s to 1.17 m/s. The shallow nozzle angle produces 10.95% spread in velocities observed while a deeper nozzle angle leads to a 4.25% spread. However, a change in nozzle angle by 10º from 25º to 35º produces a 17.6% higher velocity on an average at the throat plane where the velocities where measured. This further confirms the sensitivity of the nozzle angle on shroud performance. The sensitivity chart points towards the diffuser also being shorter in length while having a shallow angle of expansion. The effect of nozzle angle and the diffuser length can be seen in Figure 41.

The diffuser length only becomes a factor as its value drops below 23 mm. Figure 42 shows the data points being tightly packed for the deeper nozzle angles as diffuser geometry effects shroud performance after the nozzle effects are entirely diminished. Thus, Figure 41 and Figure 42 show a sharp increase in velocity for the narrow nozzle angle, diffuser angle and shorter diffuser length. Figure 43 shows relationship between diffuser length, nozzle angle and maximum recorded velocity.

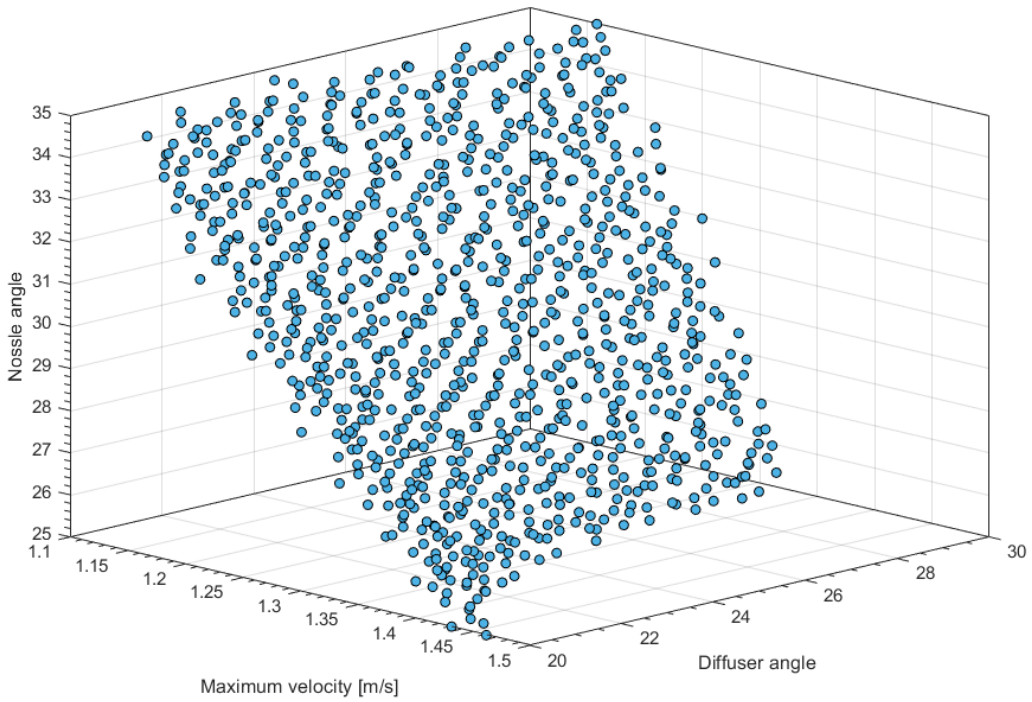


Figure 43: Relation between the diffuser length, nozzle angle and maximum recorded velocity.

The optimization of the shrouds proved the following:

- A need to have a shallow nozzle angle to not cause recirculation regions while transitioning from nozzle to the diffuser.
- The smoother transition from the nozzle to diffuser would allow for a broader operational region for the blade.
- The diffuser must expand with a shallow gradient to not allow flow field to separate and constrict the expansion region.
- This shallower expansion region is needed to match the pressure in the flow field around the shroud.

With these observations in mind, a further shroud optimisation study was conducted. The objective of the study was to design a shroud geometry for the CT-HKT to produce the maximum velocity through the rotor. A parametric model was developed in Solidworks, shown in Figure 44. The shroud geometry is defined using 7 points in space. Each point was bounded by a set of boundary conditions. For each iteration, when the values of the governing points are set, the geometry is rotated across the central axis. The geometries, which result in the maximum velocity through the shroud, are listed in the Table 16. The maximum velocity was measured between points L2 and L6.

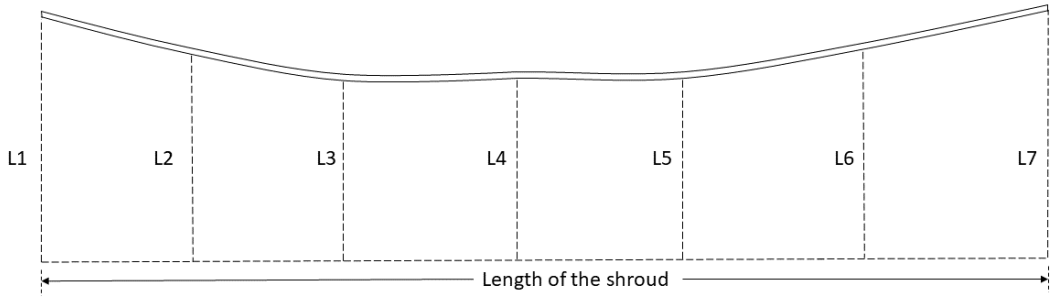


Figure 44: The shroud optimised for the field prototype of the single rotor tethered CT-HKT. The boundary conditions for the dimensions for this shroud were set using the results of the previous cases.

Table 16: Dimensions for the top 4 candidates for geometry optimised shrouds with the maximum increase in velocity reported.

| L1 [m] | L2 [m] | L3 [m] | L4 [m] | L5 [m] | L6 [m] | L7 [m] | Percentage Velocity Increase |
|---|---|---|---|---|---|---|---|
| 0.402 | 0.402 | 0.348 | 0.348 | 0.348 | 0.348 | 0.402 | 70.2 |
| 0.402 | 0.348 | 0.348 | 0.348 | 0.402 | 0.348 | 0.402 | 62.04 |
| 0.402 | 0.348 | 0.348 | 0.348 | 0.348 | 0.402 | 0.402 | 55 |
| 0.402 | 0.348 | 0.402 | 0.348 | 0.348 | 0.348 | 0.402 | 50.78 |

We conclude that adding the shroud for winter low flow operations can allow the CT-HKT to produce design point power at a reduced flow velocity of 1.2m/s, while adding system complexity as a shroud is not easy to add. It is understood that the CT-HKT would be designed to handle the maximum flow without the shroud for spring and summer high flow conditions and the shroud would only be added for the winter season.

## 4.2 Winglets

The add-on winglets were designed with multiple variable parameters shown in Figure 45. These parameters are labelled in the illustration below. The boundary condition for the optimization are given in Table 17 and were selected based on the proximity of the blade from the chassis of the supporting structure. A specific set of boundary conditions lead to an open geometry. Thus, those candidate points where eliminated from the optimization matrix. The simulations were run to stall conditions where the rotation of the blade was frozen.

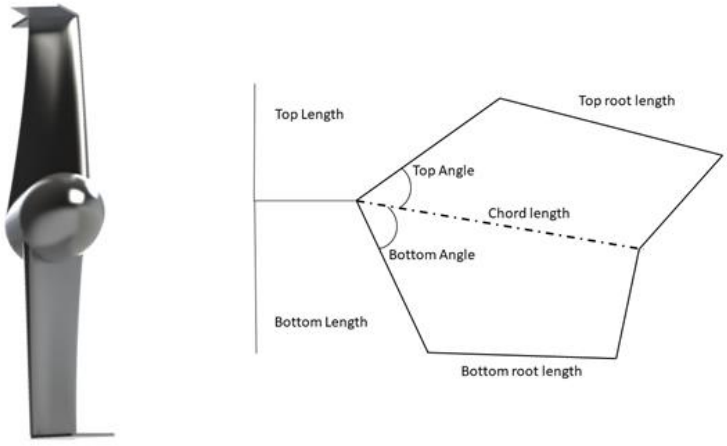


Figure 45: The CAD and the schematic parameters defining the winglet, which is to be retrofitted to the existing impeller.

Table 17: Boundary conditions set for optimizing winglets to produce maximum torque.

| Parameter | Min | Max |
|---|---|---|
| Flow field velocity | 2.0 m/s | |
| Top angle | 25º | 50º |
| Top root length | 2 mm | 30 mm |
| Top length | 20 mm | 40 mm |
| Bottom angle | 20º | 55º |
| Bottom root length | 2 mm | 30 mm |
| Bottom length | 20 mm | 55 mm |

The simulation was run over 1100 candidate points and the 3 candidates with the highest torque value are listed in Table 18.

Table 18: The optimized dimensions for the 3 candidates along with defining parameters of winglets with the maximum increase in torque.

| no | Top angle (Degree) | Top root length (mm) | Top length (mm) | Bottom angle (Degree) | Bottom root length (mm) | Bottom length (mm) | Torque (N-m) | Increase in torque |
|---|---|---|---|---|---|---|---|---|
| 1 | 25 | 30 | 40 | 38.2 | 17.02 | 43.08 | 8.09 | 10.57% |
| 2 | 26.85 | 28.62 | 39.69 | 28.0 | 13.27 | 49.68 | 8.07 | 10.34% |
| 3 | 28.97 | 28.14 | 38.26 | 41.5 | 27.19 | 27.17 | 8.05 | 10.07% |

Figure 47 shows the reduction in the spread of the data points as the front angle reduces. This is because, at a higher angle, the winglet performance gets affected by the other governing parameters, as in Figure 47. A shallow front angle also covers more projected cord length at the maximum height of the winglet. This higher coverage allows for more of the high pressure produced by the wing due to the obstruction of the flow field to be exploited.

Figure 46 shows the sensitivity analysis for the governing parameters comprising the

winglet geometry. The winglet saw no effect on performance due to the changes to the bottom length and width of the winglet. The top of the winglet, however, trended towards being tall and wide with a shallow front angle. This is seen as the winglet tries to capture the maximum amount of pressure exerted on the wing. If the winglet were any smaller, the high pressure would wrap around the blade, producing tip vortexes, as discussed in Section 2.4.

Table 18: The optimized dimensions for the 3 candidates along with defining parameters of winglets with the maximum increase in torque.

| no | Top angle (Degree) | Top root length (mm) | Top length (mm) | Bottom angle (Degree) | Bottom root length (mm) | Bottom length (mm) | Torque (N-m) | Increase in torque |
|---|---|---|---|---|---|---|---|---|
| 1 | 25 | 30 | 40 | 38.2 | 17.02 | 43.08 | 8.09 | 10.57% |
| 2 | 26.85 | 28.62 | 39.69 | 28.0 | 13.27 | 49.68 | 8.07 | 10.34% |
| 3 | 28.97 | 28.14 | 38.26 | 41.5 | 27.19 | 27.17 | 8.05 | 10.07% |

Figure 47 shows the reduction in the spread of the data points as the front angle reduces. This is because, at a higher angle, the winglet performance gets affected by the other governing parameters, as in Figure 47. A shallow front angle also covers more projected cord length at the maximum height of the winglet. This higher coverage allows for more of the high pressure produced by the wing due to the obstruction of the flow field to be exploited.

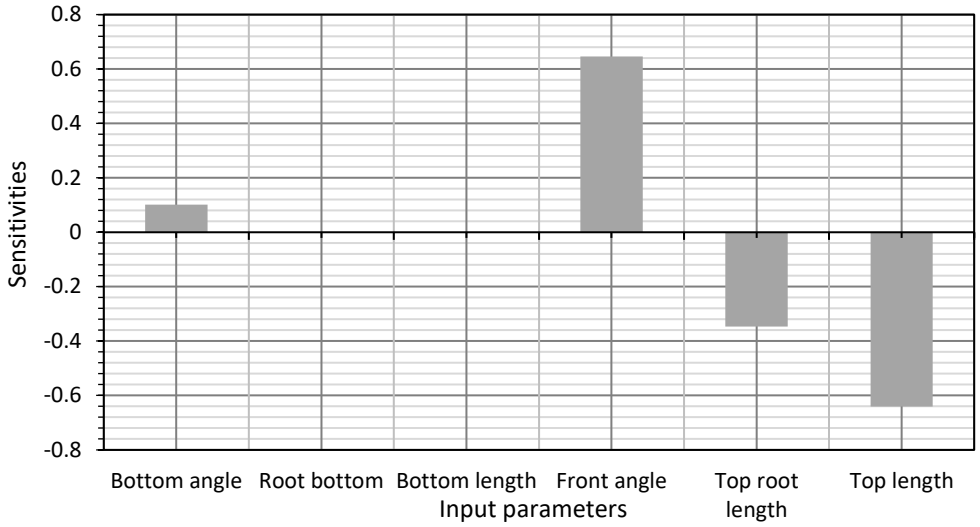


Figure 46: Sensitivity analysis showing the effects of each parameter on the maximum torque recorded during the iterations of parameters defining the winglets.

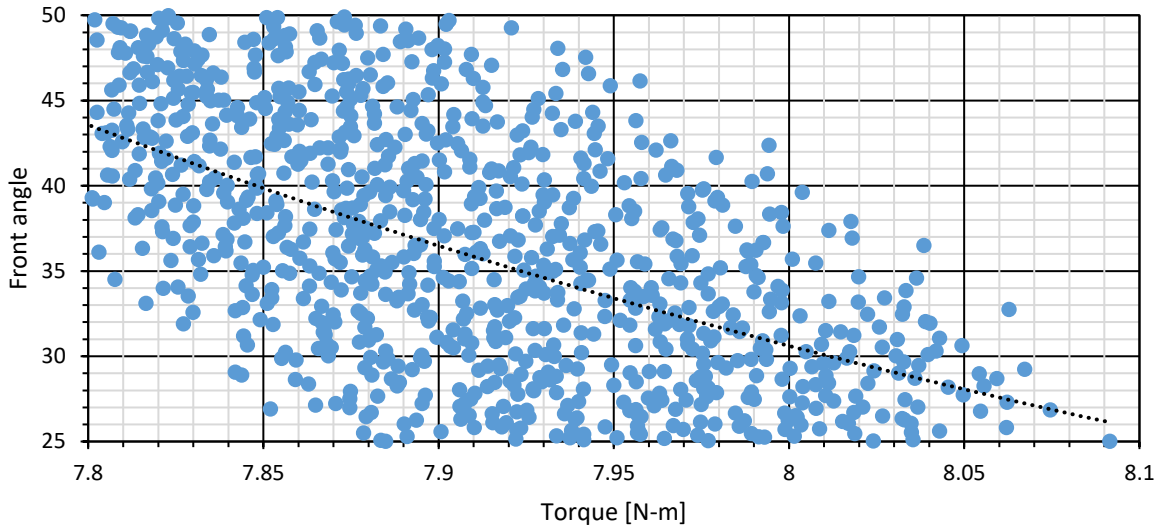


Figure 47: The increases in the torque value plotted with respect to the change in front angle. Note the reduction in spread for torque valves as the front angle decreases.

Figure 48 shows the top root length normalised with respect to chord length. This was done to get a close relationship between the designed impeller and add-on components, if needed. The relationship can be used as a starting point for future add-on component design. The normalised top length shows the tight spread in the data points at the higher

torque values of around 27-31% of the chord length. It is critical to note a longer top root length will result in a higher torque. As geometries with a longer top root length trap more pressure, thus resulting in more torque. Figure 48 shows the normalised top height concerning the length of the blade. The trend shows that the higher winglet height traps more pressure, thus leading to higher torque. This trend starts to plateau once the winglet height reaches 13% of the blade length. The maximum torque value when the winglet height is 7% of the blade length is 7.92 N-m; whereas if the winglet height is 14% of the blade height is 8.09 N-m. Thus, it shows the law of diminishing marginal returns in keeping with the trendline.

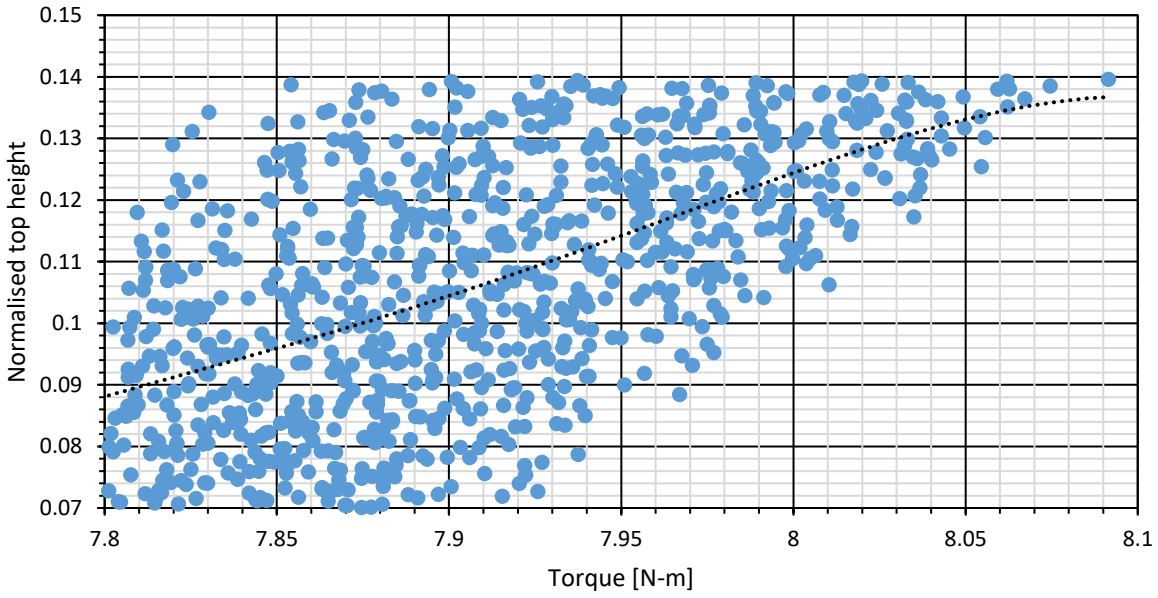


Figure 48: The normalised top height with respect to the impeller length vs the recorded torque.

Normalised top length in Figure 49 shows for an initial increase of 23.33% in normalised top root length the torque increases by 2.5%. However, for to get a further 1.2% the normalised top root length must increase by 36.9%. A larger footprint of winglets leads to a larger velocity defect around the blade.

Figure 50 shows the velocity defect around the impeller before and after the winglet is installed. It was observed at operational RPM the torque produced by the blade was 10% lower than when the blade was without the winglet. The reason is the velocity defect around the impeller is more substantial and surrounds the impeller completely when compared to the winglet-less impeller as can be seen in

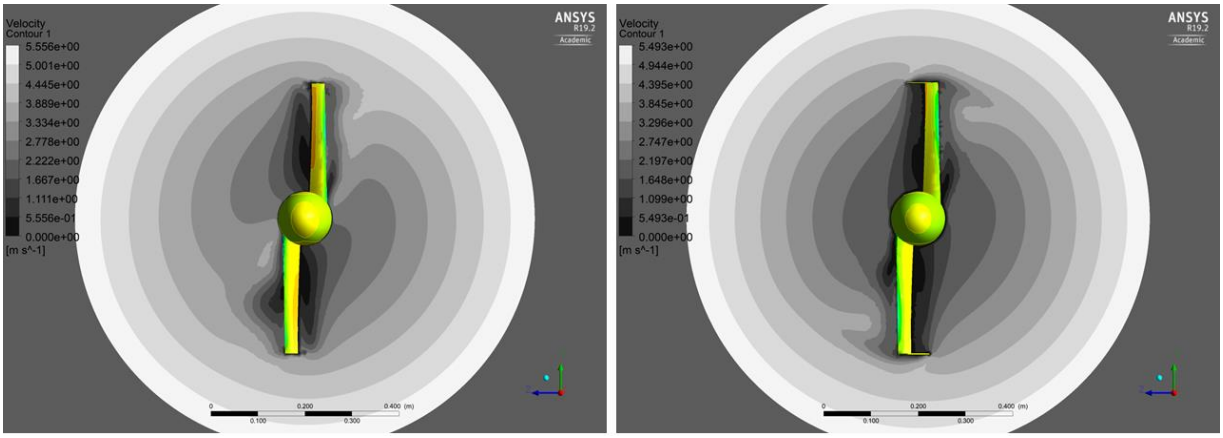


Figure 50.

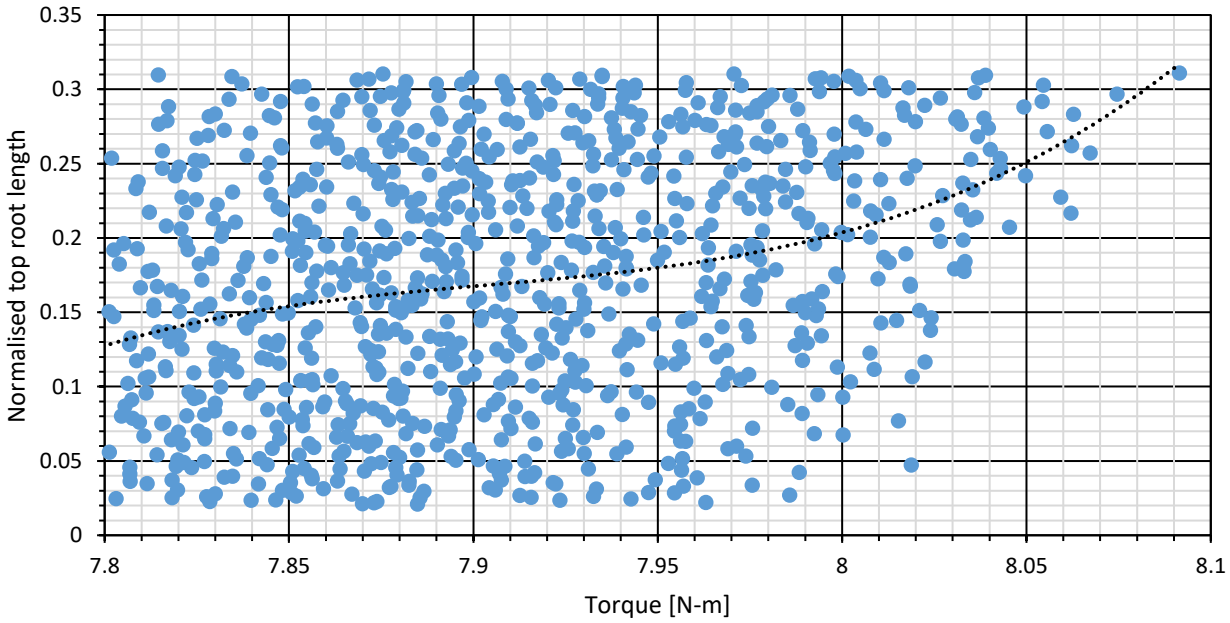


Figure 49: The normalised top root length with respect to the chord length shows increase

in torque becomes minimal past the 27% of blade length.

The increased velocity defect results in the second blade experiencing wake produced by the motion of the 1st blade, thus encountering less fluid pressure with leads less overall torque. The velocity defect was not considered in this research.

From the results winglets cannot address low flow winter conditions by itself, as it improves turbine efficiency by only 10%.

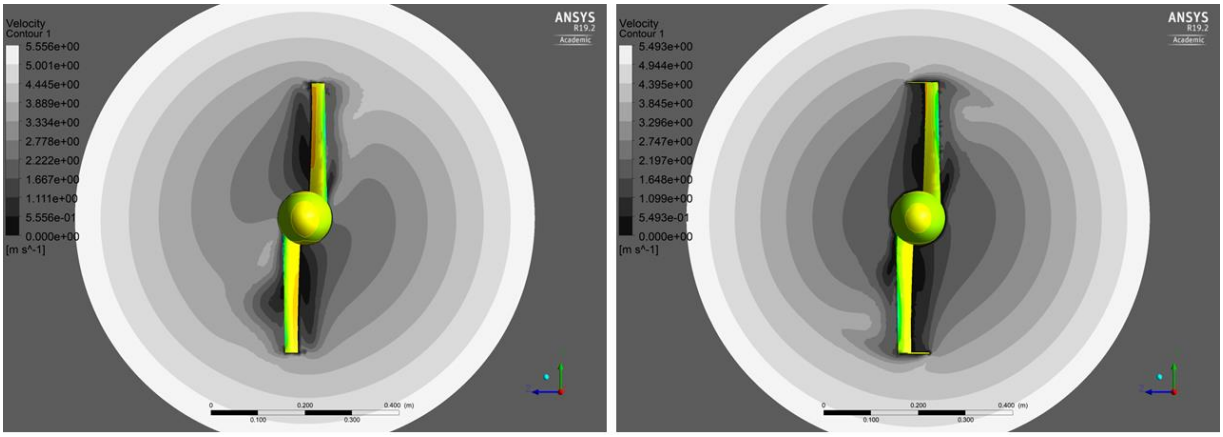

Figure 50: The comparison in the rotating frame of reference between a blade without winglets and with winglets. The increase in velocity defect around the blade causes the operational torque valve to drop.

## 4.3 Advantages of optimised add-on components over impeller extension

Optimised add-on components allow CT-HKT to achieve design point power and torque at lower velocities than designed operational velocity. However, this is not the only method to attain design point characteristics, extending impeller length can provide the same effect. A boat could go and bring the turbine to the surface and bolt on 3 blade extension for winter operations as an example.

To highlight the advantages of add-on components a comparison between different add-on components and impeller extension is given in Table 19.

Table 19: The advantages of add-on components to impeller extension.

| Parameter | Lowest velocity that can sustain design point conditions (m/s) | Impeller diameter required for design point conditions at the highlighted velocity (m) |
|---|---|---|
| Power | 1.25 | 1.160 |
| Torque | 1.8 | 0.645 |

Table 19 shows the following aspects:

- CT-HKT with the aid of the optimised shroud can produce design point power at 1.25 m/s. The impeller diameter required to produce design point power at 1.25 m/s would be 1.160 m. This diameter is 2 times bigger than the originally designed impeller.
- CT-HKT with the help of winglets can produce design point torque at 1.8 m/s. To sustain design point torque at lower values the impeller diameter would have to increase by a factor of 1.125 to 0.645 m.

An impeller this large would require a redesign of the CT-HKT system. This redesigned CT-HKT system would have a larger footprint and a lower capacity factor.

# 5. Testing results at the CHTTC

A parametric performance matrix is developed to test the operational performance of various systems involved in the field prototype of the CT-HKT. The tests are carried out at the CHTTC downstream of the Seven Sister Generation station. The CT-HKT system is tested for flotation and dive capability in no-flow and highly energetic river, electrical power output. The power produced by the generator was to be measured by a multi-meter with readings taken every minute.

## 5.1 Launch procedure and set-up

The CT-HKT system is mounted to a boat trailer. The CT-HKT system is mounted on a trailer supported by two 4x4 beams and taken to site for test. The two 4X4 beams are used to deploy the CT-HKT system to provide extra buoyancy in case the flotation system failed. The trailer is backed into a bay of low-velocity currents, called Jackfish Bay. This location was selected for the initial launch of the CT-HKT system as the depth of the boat launch is less than 2 m. Once the trailer is retrieved from the boat launch, the CT-HKT is towed near the operation platform using a safety rope. After the CT-HKT system reaches close to the operational platform, the mooring system is attached, and the beams are removed from the CT-HKT. Allowing the HKT system to float on self-buoyancy is shown in Figure 51. This successfully concludes the float test for the CT-HKT.

Figure 51: The CT-HKT being launched at the Jackfish Bay. The figure shows both 4X4 beams underneath the HKT as it launched for the first time.

## 5.2 Jackfish bay testing

Having completed the float test, the CT-HKT system and the operating platform were set up to evaluate the functioning of the pneumatic control system installed to modulate the buoyancy. In the initial set-up, the water-in one-way pressure valve was at the bottom of the active ballast whereas the water-out one-way valve was at the top. When system was de-pressurised by the vacuum pump to -10 in of Hg. The control system reacted favourably allowing the water to flow into the buoyancy control system. However, the system could not expel the water, therefore the buoyancy system was altered to have the water-out one-way valve to be at the bottom and water-out one-way valve to the top. A tube was attached to the water in one-way pressure valve to allow for continuous contact with water.

Following the change, the CT-HKT system can both decrease and increase the buoyant

force exerted by the CT-HKT system by modulating the volume of water inside the active ballast. The operational platform is now anchored to an existing underwater anchor. The CT-HKT system is now set for an operational dive test. The vacuum pump is operated to maintain -10 in of Hg. As the buoyancy of the CT-HKT system started to decrease the CT-HKT system started to tilt towards the operational configuration. The test had to be abandoned due to loss of vacuum which resulted in the water entering the vacuum side of the control system.

The water inside the CT-HKT system was let out using the compressed air. The vacuum pump control line was modified to include a water-air separator and vacuum pump had to be drained of all the water and re-filled with oil.

The modified control system circuit is now returned to the CHTTC. A new test for CT-HKT system was conducted using the boat launch at Pinawa Bridge as launch facility at Jack-fish bay flooded. The distance between Pinawa Bridge and Jackfish bay is 2.25 km as shown in Figure 52. The CT-HKT was attached to the operational platform using the designed mooring system and towed to Jackfish bay. The CT-HKT system is prepared for operation with the vacuum pump is set to regulate at -10 inch of Hg. The CT-HKT system can take in water to increase the mass of the system. As the waterline crossed the centre line of the impeller, the impeller came off the shaft and had to be retrieved using a hook. The dive operation was continued as planned at this point but after a few minutes, the system started tipping forwards. Some detachable weight was added to the back of the CT-HKT to maintain level. However, after taking in

approximately 40 Litres of water, the CT-HKT tipped forwards aggressively. Due to the aggressive tilt water came entered the vacuum side of the control unit but the presence of the water-air separator checked water from reaching the vacuum pump. As the CT-HKT system tilted past 30° as shown in Figure 53, the experiment was called off. The water removal protocol was initiated, and the turbine towed back to the boat launch at the Pinawa Bridge.


Figure 52: The path taken by the blue pontoon to the jackfish bay from the deployment site at the Pinawa Bridge. This was done as the boat launch at the Jackfish bay was obstructed by the Aluminium Pontoon and a crane.

## 5.3 Test observations

The impeller separated from the shaft as the water crossed the centre point of the impeller hub. The water crossing the half-way mark on the impeller caused the buoyant force to push the already damaged hub upwards thus making it come loose. Further analysis showed that due to the continuous forces acting on the hub while the turbine was spinning caused the 3D printed hub to be shear because of the keys holding the blade to the shaft.

Testing was designed to check for the stability of the CT-HKT system while undergoing the process to alter the buoyancy state of the CT-HKT system. To allow for the buoyancy change to take place the mass in the form of surrounding water was added to the control volume. The water is allowed to enter by opening a one-way pressure valve at -10 inch of Hg. As the valve was opened water entering CT-HKT system moves towards the low-pressure region near the control chord. As the experiment continues, the disproportionate amount of mass accumulates at the front end of the nacelle causing the CT-HKT to tip forwards as was observed during the test. The process of forward tipping is depicted in Figure 53.

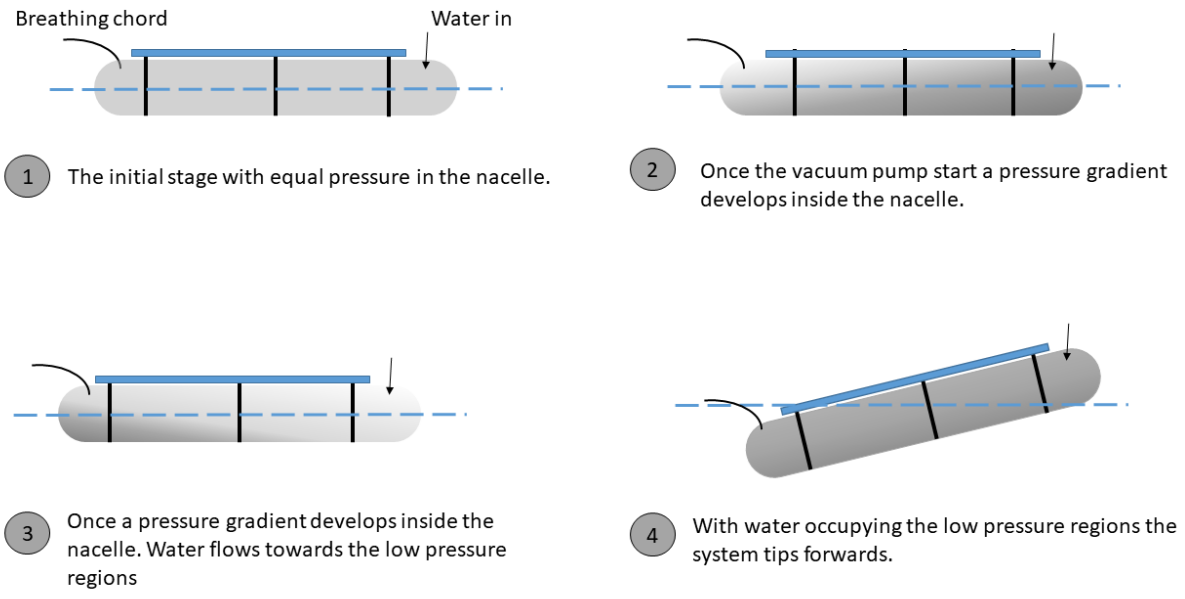


Figure 53: The details of the pressure gradients and water accumulation that caused the CT-HKT to tip forwards.

To address the issues observed during testing of the CT-HKT, the following design changes have been proposed to the active ballast and control system.

- The active ballast was initially designed to be a single cavity; however, after the testing, the active ballast was sub-divided into 7 chambers. Each chamber is designed to have 3 holes to mount one-way valves. The water-out valve would be at the lowest point in ballast. The pressure modulation port is 20º off from the top center whereas the water in port is 20º to the other side of the top center. The water in port is still to be connected to a feed tube to maintain contact with water and allow for entry to active ballast. The redesigned active ballast is shown in Figure 54.

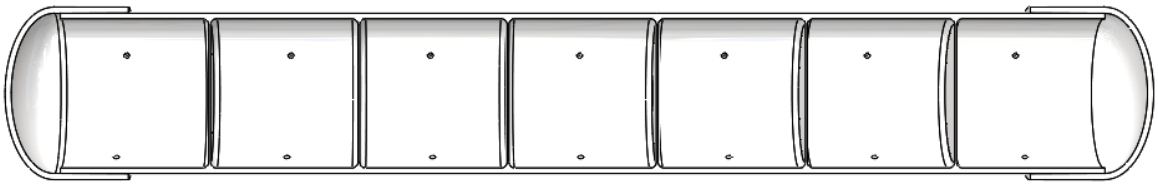

Figure 54: Cut section of the modified active ballast with separate cavities. Each cavity has a separate water-in port, water-out port, and pressure modulation port.

The control system is also modified need changes to fill the cavities and to allow for system stability automatically. The schematic diagram for the redesigned control system is shown in

- Figure 55. The control system tested comprised of manual mechanical valves. These valves would be replaced by a host of solenoid valves operated by a single controller. The chamber would also be equipped with a sensor unit to determine

the amount of water inside the cavity. The controller would then modulate the pressure in the chamber as required. This allows the system can maintain stability and can provide fine control during the operation.

- The amount of water required in the cavities can be set to a predetermined valve or can be linked with depth change and power produced.

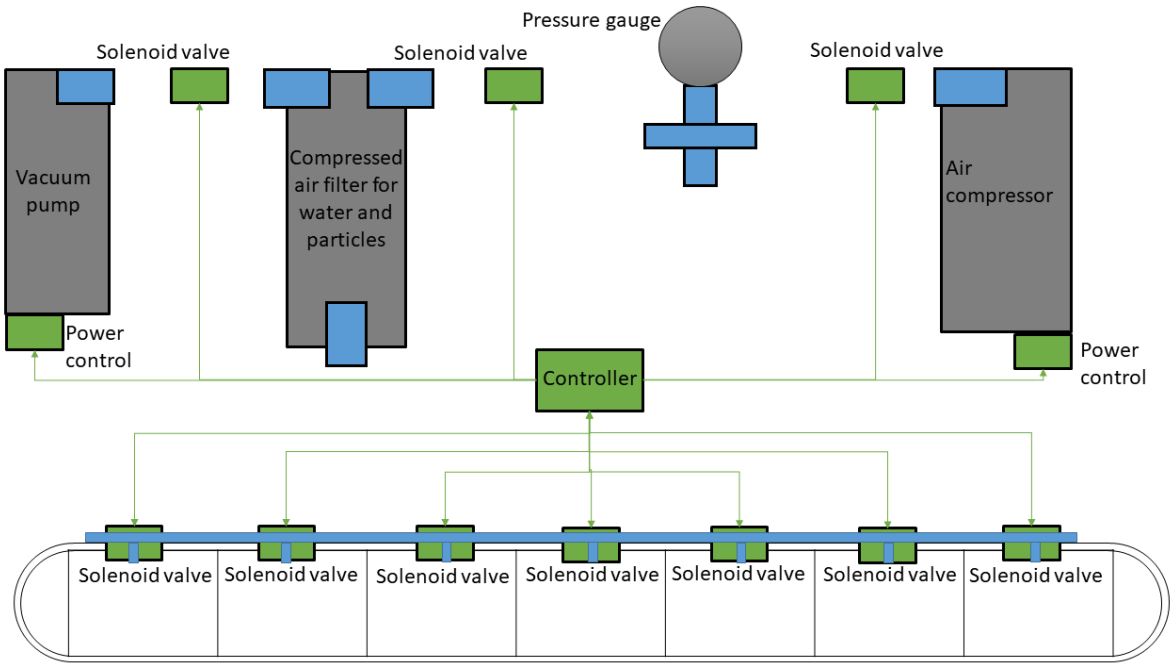


Figure 55: The schematic of the conceptual control system. The control system uses a control unit to modulate the pressure in the active ballast. The pressure modulation is done by altering the power state of the power controllers attached to vacuum pump and air compressor. The solenoid valves controlled by the controller allow for operational stability of the CT-HKT.

Sensors that can be used to report the amount of water inside each cavity accurately are listed below.

1. Float which operates on Archimedes' principle as the level of water rises in the

cavity the force acting on the float changes; the changes in force are measured by a transducer and reported to the controller.

2. Ultrasonic sensors operate based on the Doppler effect. The sensor system is devoid of moving components, has very high sensitivity as measurements can be recorded at 60 Hz. However, this system is depended on the pressure inside the cavity.
3. Laser level works like the ultrasonic sensor, but instead of sound, the laser level sensor uses short bursts of laser lights.

Other sensors such as load cell and capacitance transmitter can also be useful, but underwater operability would require substantial design changes. The controller unit can base on an Arduino board and would require developing a program to control the pressure changes in the active ballast to provide stable operating conditions. The pressure modulation can be achieved by changing power states on the vacuum pump and the air compressor. The blade on closer inspection was deemed to be damaged due to the shear forces acting at the pinch points. The blade was redesigned using an aluminium sleeve to add more structural strength. The differences between the initial CAD model and revised CAD model are shown in Figure 56.

Figure 56

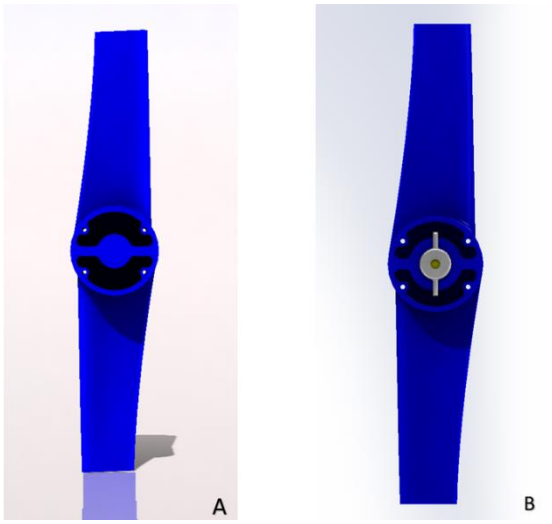


Figure 56: a) The blade that was tested at the CHTTC, and b) the modified blade designed to address issues discovered during in-situ tests conducted at CHTTC.

# 6. Conclusion

This thesis presents CFD analysis for add-on components that can improve the performance of the CT-HKT during low flow regimes that occur either due during winter or drought years. The CFD mesh was validated by comparison against experimental data. The thesis highlights the unintended effects of winglets during operation. The thesis also presents two consolidated numerical models that can be used to arrive at dimensions for future CT-HKTs. However, it is essential to state that this design did away with a less obtrusive design of the water tunnel prototype. Incorporating an optimised design of ballasts can reduce the wake of the CT-HKT or use the ballasts as shrouds to accelerate flow velocities. This would require optimization with transient flow regimes. Such an optimization would be computationally time intensive because of the fine resolution required optimising locus of the ballasts while reducing the effects of wake caused behind the CT-HKT. This research demonstrates that an HKT based upon counter-torque mechanism is more accessible, potentially cost-effective to deploy and retrieve, can dive out of the way of debris and year-round operability. Thus, making CT-HKT system it is an attractive proposition for Northern off-grid communities.

The thesis presents evidence that an CT-HKT can accomplish the followings:

1. The CT-HKT, when coupled with a control system, can work in winter conditions by avoiding operation in the air-water interface region. This would remove the possibility of the HKT forming large icebergs and sinking due to damage to the structure of the HKT.
2. As the CT-HKT can operate in harsh winter conditions, the operation time of the

CT-HKT doubles over a conventional near-surface HKT. Thus, leading to the CT-HKT producing more units of electricity than its conventional substitute.

3. The design and optimization of add-on components results in the CT-HKT's ability to operate in lower than design point flows. This aids the CT-HKT to produce design point power in the low flow regimes, especially during winter seasons.
4. The CT-HKT presented in the thesis can be deployed using the boat launches as a typical zodiac boat. The ease of deployment due to lack of special equipment like a crane or barge results in lower costs of deployment as specialised skilled manpower is not needed.

**Recommendations and future work**

The conceptual design is a schematic of the modifications that would improve the technological readiness of the CT-HKT. These modifications would require the inclusion of sensors to measure depth and power produced. The control system would also need to have fall back mechanism in case the controls fail due to unforeseen circumstances. The components used in the control system viz vacuum pump and air compressor would need to be optimised to not have a significant parasitic loss on the power produced by the CT-HKT. Another area of optimization would be the geometry of the ballasts. Ballasts can be optimised either to have reduced wake allowing more turbines to operate at a select HKT site or the ballasts produce accelerated flow to produce more power from the same turbine. CFD simulations can be run on blade, shroud, and winglet geometries with more variables to optimise the add-on components for the CT-HKT.

## 7. Bibliography

[1] James Knowles, “Power Shift: Electricity for Canada’s Remote Communities,” The Conference Board of Canada, Ottawa, Sep. 2016. [Online]. Available: http://www.conferenceboard.ca/e-library/abstract.aspx?did=8249.

[2] U.S. Environmental Protection Agency, “Climate Change Indicators in the United States 2016,” U.S. Environmental Protection Agency, Washington, D.C., EPA 430-R-16-004, 2016. [Online]. Available: www.epa.gov/climate-indicators.

[3] Regie de l’energie and Hydroquebec, “Hydroquebec Electricity Rates,” Hydroquebec, Montreal, Quebec, D-2019-037, 2019. [Online]. Available: http://www.hydroquebec.com/data/documents-donnees/pdf/electricity-rates.pdf?v=20190401.

[4] Manitoba Hydro, “Proposed rates and customer imapcts,” Manitoba Hydro, Winnipeg, Manitoba, Jan. 2015.

[5] British Columbia Hydro and Power British Columbia Hydro and Power Authority, “British Columbia Utilities,” British Columbia Utilities Commission, Vancover, 2016.

[6] Hydro One, “Electricity pricing and derivatives,” *Electricity Pricing and Costs*. https://www.hydroone.com/rates-and-billing/rates-and-charges/electricity-pricing-and-costs (accessed Jun. 17, 2020).

[7] Natural Resources Canada and Indigenous and Northern Affairs Canada, “Remote Communities Energy Database,” *Nat. Resour. Can.*, no. 2019, 2019, [Online]. Available: https://atlas.gc.ca/rced-bdece/en/index.html.

[8] Natural Resources Canada and Indigenous and Northern Affairs Canada, “Remote Communities Database,” *Nat. Resour. Can.*, no. 2019, 2019, [Online].

Available: http://atlas.gc.ca/rced-bdece/en/index.html.

[9] Standing Senate Committee on Energy the Environment and Natural Resources, “Powering Canada’s Territories,” Parliament of Canada, Ottawa, 2014.

[10] M. J. Khan, G. Bhuyan, M. T. Iqbal, and J. E. Quaicoe, “Hydrokinetic energy conversion systems and assessment of horizontal and vertical axis turbines for river and tidal applications: A technology status review,” *Appl. Energy*, vol. 86, no. 10, pp. 1823–1835, 2009, doi: 10.1016/j.apenergy.2009.02.017.

[11] S. D’Auteuil, “Investigation and Development of Flow and Turbulence Measurement Techniques for Riverine Hydrokinetic Turbine Sites by,” The University of Manitoba, Winnipeg, Manitoba, 2017.

[12] S. Kassam, “In-Situ Testing Of A Darrieus Hydro Kinetic Turbine in Cold Climates,” The University of Manitoba Thesis, Winnipeg, Manitoba, 2009.

[13] Clean Current Power Systems, “Clean Current Power Systems Incorporated,” Vancover, 2004, no. June.

[14] M. F. Chow, M. A. bin Bakhrojin, H. Haris, and A. A. A. Dinesh, “Assessment of Greenhouse Gas (GHG) Emission from Hydropower Reservoirs in Malaysia,” in *Proceedings*, Malaysia, Nov. 2018, vol. 2, pp. 1380–1380, doi: 10.3390/proceedings2221380.

[15] M. A. Paucar, P. I. Amancha, T. D. San Antonio, L. P. Acurio, A. F. Valencia, and C. Galarza, “Methane Emissions from Ecuadorian Hydropower Dams,” in *IOP Conference Series: Earth and Environmental Science*, Ecuador, 2018, vol. 151, p. 7, doi: 10.1088/1755-1315/151/1/012002.

[16] S. E. Ben Elghali, M. E. H. Benbouzid, and J. F. Charpentier, “Marine tidal current

electric power generation technology: State of the art and current status," *Proc. IEEE Int. Electr. Mach. Drives Conf. IEMDC 2007*, vol. 2, pp. 1407–1412, 2007, doi: 10.1109/IEMDC.2007.383635.

[17] A. Hamta, "A Remotely Operated Hydrokinetic Turbine to Reduce the Levelized Cost of Energy of Marine Turbines by," 2016.

[18] Joseph Salvatore, "World Energy Perspective - Cost of Energy Technologies," World Energy Council, New York, 4184478, 2013. [Online]. Available: http://www.worldenergy.org/wp-content/uploads/2013/09/WEC_J1143_CostofTECHNOLOGIES_021013_WEB_Final.pdf.

[19] Canadian Hydraulics Centre, "Assessment of Canada's Hydrokinetic Power Potential: Phase I Report Methodology and Data Review," 2010.

[20] M. Gabriel, F. Joseph, L. William, and R. Jairo, "The Allocation of Kinetic Hydro Energy Conversion Systems (KHECS) in USA Drainage Basins: Regional Resource and Potential Power.," Palo Alto, Aug. 1986, p. 80.

[21] UMA Group, "An Evaluation of The Kinetic Energy of Canadian Rivers & Estuaries. Technical report, Canadian National Research Council," Mar. 1980.

[22] NRC-CHC, "Methodology for the assessment of hydraulic kinetic energy in rivers.," National Research Council - Canadian Hydraulics Centre, Ottawa, CHC-CTR-075, Mar. 2008.

[23] J. Bomhof, "Estimating Flow, Hydraulic Geometry, and Hydrokinetic Power at Ungauged Locations in Canada," University of Ottawa, Ottawa, 2014.

[24] Canadian Hydrokinetic Turbine Test Centre, "Canadian Hydrokinetic Turbine

Test Centre Safe Work Procedures," no. March, pp. 52–52, 2017.

[25] A. H. Birjandi and E. L. Bibeau, "Improvement of Acoustic Doppler Velocimetry in bubbly flow measurements as applied to river characterization for kinetic turbines," *Int. J. Multiph. Flow*, vol. 37, no. 8, pp. 919–929, 2011, doi: 10.1016/j.ijmultiphaseflow.2011.05.001.

[26] The World Bank, "Electric power consumption (kWh per capita) | Data," International Energy Agency, Paris, France, Data bank, 2014.

[27] N. Jackimec and R. Vaid, "Hydrokinetic energy assessment in the Winnipeg River system," Nova Scotia, 2018.

[28] J. Woods, "Hydrokinetic Turbine Systems for Remote River Applications in Cold Climates," The University of Manitoba, Winnipeg, Manitoba, 2017.

[29] A. Hamta, "A Remotely Operated Hydrokinetic Turbine to Reduce the Levelized Cost of Energy of Marine Turbines by," The University of Manitoba, Winnipeg, Manitoba, 2016.

[30] W. Short, D. Packey, and T. Holt, "A manual for the economic evaluation of energy efficiency and renewable energy technologies," National Renewable Energy Laboratory, Golden, Colorado, AS026100, Mar. 1995. [Online]. Available: http://large.stanford.edu/publications/coal/references/troughnet/market/docs/5173.pdf.

[31] IT Power and Jeremy Thake, "Development, installation and testing of a large scale tidal current turbine," DTI Technology programme, North Devon, URN 05/1698, Oct. 2005.

[32] A. H. Birjandi, S. D'Auteuil, C. Ridd, and E. L. Bibeau, "An innovative low cost hydrokinetic site selection technique for cold climate regions," 2015, doi:

10.1109/OCEANS-Genova.2015.7271660.

[33] B. Wang, Z. J. Lu, X. B. Chen, P. Wang, W. Luo, and H. Xu, “Modeling and analysis of the dynamic efficiency of manual transmission/reducer,” *Int. J. Automot. Technol.*, vol. 16, no. 3, pp. 417–426, Jun. 2015, doi: 10.1007/s12239-015-0043-0.

[34] Y. M. Buzin, “Mechanical efficiency of a transportable vehicle,” Voronezh Gas State University, Voronezh, 2011.

[35] J. Liebrecht, X. Si, B. Sauer, and H. Schwarze, “Investigation of drag and churning losses on tapered roller bearings,” *Strojniski VestnikJournal Mech. Eng.*, vol. 61, no. 6, pp. 399–408, 2015, doi: 10.5545/sv-jme.2015.2490.

[36] A. Dolgushin, D. Voronin, and O. Mamonov, “Optimization of Resource Consumption When using Vehicle Transmissions at Low Temperatures,” *J. Eng. Appl. Sci.*, vol. 15, no. 1, pp. 74–80, Oct. 2019, doi: 10.36478/jeasci.2020.74.80.

[37] A. Betz, *Introduction to the Theory of Flow Machines. [1st English ed.]. Oxford*, 1st ed. Michigan: Pergamon Press, 1966.

[38] L. Mahrt, J. Sun, and D. Stauffer, “Dependence of Turbulent Velocities on Wind Speed and Stratification,” *Bound.-Layer Meteorol.*, vol. 155, no. 1, pp. 55–71, Apr. 2015, doi: 10.1007/s10546-014-9992-5.

[39] S. O. Hansen, “Vortex-induced vibrations of structures,” in *Structural Engineers World Congress 2007*, Bangalore, Nov. 2007, vol. 48, p. 20.

[40] K. Fischer, F. Besnard, and L. Bertling, “Reliability-Centered Maintenance for Wind Turbines Based on Statistical Analysis and Practical Experience,” *IEEE Trans. Energy Convers.*, vol. 27, no. 1, pp. 184–195, 2012, doi: 10.1109/TEC.2011.2176129.

[41] V. S. Neary *et al.*, “Methodology for Design and Economic Analysis of Marine

Energy Conversion (MEC) Technologies," *Sandia Natl. Lab.*, no. March, pp. 261–261, 2014.

[42] D. S. Jenne, Y. Yu, and V. Neary, "Levelized Cost of Energy Analysis of Marine and Hydrokinetic Reference Models Preprint," no. April, 2015.

[43] New energy corporation, "Power Units - New Energy Corporation - A Leading Manufacturer and Developer of Hydrokinetic Turbines."

[44] V. S. Neary *et al.*, "Methodology for Design and Economic Analysis of Marine Energy Conversion (MEC) Technologies," *Sandia Natl. Lab.*, no. March, p. 261, 2014.

[45] Dehlsen Associates and A. J. Fleming, "Aquantis Ocean Current Turbine Development Project Report," no. June, 2014, doi: 10.2172/1150234.

[46] BlueTEC, "BlueTEC Philosophy – Bluewater," *Bluewater's Tidal Energy Converter*, 2015. https://www.bluewater.com/products-technology/floating-tidal-systems/new-energy/emec/bluetec-phil/ (accessed Jun. 13, 2019).

[47] EMEC, "EMEC: European Marine Energy Centre - Orkney," [Online]. Available: http://www.emec.org.uk/index.asp%5Cnhttp://www.emec.org.uk/downloads.asp%5Cn http://www.emec.org.uk/national_standards_abstracts.asp%5Cnhttp://www.emec.org.uk/people.asp.

[48] F. G. Becker, "Deep Green holyhead deep project phase I," Minesto AB, United Kingdom, Environmental Impact Assessment L-100194-S14-EIAS-002, Jun. 2016.

[49] Bourne Energy, "Bourne Energy's RiverStar," *Bourne Energy's RiverStar*, 2015. http://www.bourneenergy.com/future.html (accessed Jun. 15, 2019).

[50] MarineEnergy.biz, "Introducing Alstom's Oceade™ 18 – 1," *Introducing Alstom's Oceade™ 18 – 1.4 MW tidal turbine*, 2015. https://www.offshore-energy.biz/introducing-

alstoms-oceade-18-1-4-mw/ (accessed Jun. 15, 2019).

[51] N. Mehmood, Z. Liang, and J. Khan, “Diffuser Augmented Horizontal Axis Tidal Current Turbines,” *Res. J. Appl. Sci. Eng. Technol.*, vol. 4, no. 18, p. 10, Jun. 2012.

[52] Ocean Flow, “Evopod™ _ Oceanflow,” 2017. http://www.oceanflowenergy.com/Evopod-Technology.html (accessed Jun. 15, 2019).

[53] A. Pacheco, E. Gorbeña, T. Plomaritis, and J. Gonçalves, “Lessons learned from E1 Evopod Tidal Energy Converter deployment at Ria Formosa, Portugal SCORE-Sustainability of using Ria Formosa Currents On Renewable Energy production View project OpTiCA-Optimisation of Tidal Energy Converter Arrays View project Less,” pp. 1–8, 2018.

[54] T. Hunt, “THOR’ s Power Method for Hydrokinetic Devices,” THOR Energy Group LLC, Cincinnati, EE0003634, Sep. 2011.

[55] Tocardo, “Tocardo T1,” *T-1 – Community Based Tidal Turbine*, 2008. https://www.tocardo.com/tocardo-t1/ (accessed Jun. 15, 2019).

[56] Tocardo, “Tocardo T2 Series,” *Tidal turbines suitable for industrial, direct wire applications*, 2014. https://www.tocardo.com/tocardo-t2/ (accessed Jun. 15, 2019).

[57] G. Holdings, “GEM Hydro-Kinetic Turbine Rivers and Oceans – gemholdings,” *GEM Hydro-Kinetic Turbine Rivers and Oceans*. https://gemholdingsltd.com/pages/hydro-kinetic-turbine (accessed Jun. 15, 2019).

[58] B. Gunawan, V. S. Neary, and J. Colby, “Tidal energy site resource assessment in the East River tidal strait, near Roosevelt Island, New York, New York,” *Renew. Energy*, vol. 71, pp. 509–517, 2014, doi: 10.1016/j.renene.2014.06.002.

[59] Hydra Tidal Energy Technology, “Hydra Tidal Energy Technology,” 2001.

https://www.linkedin.com/company/hydra-tidal-energy-technology-as/ (accessed Jun. 15, 2019).

[60] Zhiyong Ma, Rui Jiang, Dameng Wang, and Kaili Zhang, “Fault mode, effects and criticality analysis for overheating fault of wind turbines gearbox and generator,” in *International Conference on Renewable Power Generation (RPG 2015)*, Beijing, China, 2015, p. 5 .-5 ., doi: 10.1049/cp.2015.0445.

[61] IEA, “Offshore Wind Outlook 2019,” 2019. [Online]. Available: https://www.iea.org/reports/offshore-wind-outlook-2019.

[62] M. Shahsavarifard, E. L. Bibeau, and V. Chatoorgoon, “Effect of shroud on the performance of horizontal axis hydrokinetic turbines,” *Ocean Eng.*, vol. 96, pp. 215–225, 2015, doi: 10.1016/j.oceaneng.2014.12.006.

[63] A. C. Aranake, V. K. Lakshminarayan, and K. Duraisamy, “Computational analysis of shrouded wind turbine configurations using a 3-dimensional RANS solver,” *Renew. Energy*, vol. 75, pp. 818–832, 2015, doi: 10.1016/j.renene.2014.10.049.

[64] A. C. Aranake, V. K. Lakshminarayan, and K. Duraisamy, “Computational analysis of shrouded wind turbine configurations using a 3-dimensional RANS solver,” *Renew. Energy*, vol. 75, pp. 818–832, 2015, doi: 10.1016/j.renene.2014.10.049.

[65] Y. Ohya and T. Karasudani, “A shrouded wind turbine generating high output power with wind-lens technology,” *Energies*, vol. 3, no. 4, pp. 634–649, 2010, doi: 10.3390/en3040634.

[66] W. Han, P. Yan, W. Han, and Y. He, “Design of wind turbines with shroud and lobed ejectors for efficient utilization of low-grade wind energy,” *Energy*, vol. 89, pp. 687–701, 2015, doi: 10.1016/j.energy.2015.06.024.

[67] S. C. Yen and Y. F. Fei, “Winglet dihedral effect on flow behavior and aerodynamic performance of NACA0012 wings,” *J. Fluids Eng. Trans. ASME*, vol. 133, no. 7, 2011, doi: 10.1115/1.4004420.

[68] N. T. Note, “Technical Note Nasa Tn D-8260 Wind-Tunnel Subsonic Mounted Approach Results Speeds for and At Selected Wing-Tip Winglets National Aeronauticsand Space Administration,” *Notes*, no. July, 1976.

[69] G. Stuart and Nasa, “A high subsonic speed wind-tunnel investigation of winglets on a representative second generation jet transport wing,” National Aeronautics and Space Administration, Washington, D.C., Technical note Nasa tn d-6846, Jul. 1976.

[70] P. D. Gall and H. C. Smith, “Aerodynamic characteristics of biplanes with winglets,” *J. Aircr.*, vol. 24, no. 8, pp. 518–522, Aug. 1987, doi: 10.2514/3.45470.

[71] G. Ingram, “Wind Turbine Blade Analysis using the Blade Element Momentum Method,” *October*, vol. 1.1, no. c, pp. 1–21, 2011.

[72] Z. Sun, J. Chen, W. Z. Shen, and W. J. Zhu, “Improved blade element momentum theory for wind turbine aerodynamic computations,” *Renew. Energy*, vol. 96, pp. 824–831, 2016, doi: 10.1016/j.renene.2016.05.035.

[73] F. Mechanics, G. F. Mechanics, and P. Contributors, “Fluid Mechanics General Fluid Mechanics Physics Contributors Baker Navier-Stokes Equations,” no. 3, 1995.

[74] P. J. Schubel and R. J. Crossley, “Wind turbine blade design,” *Energies*, vol. 5, no. 9, pp. 3425–3449, 2012, doi: 10.3390/en5093425.

[75] M. J. Clifton-Smith, “Wind Turbine Blade Optimisation with Tip Loss Corrections,” *WIND Eng.*, vol. 33, no. 5, pp. 477–496, 2009.

[76] U. S. E. I. Administration, “Electric Power Monthly with Data for October 2019,”

no. December, pp. 1–772, 2019.

[77] Y. El Khchine and M. Sriti, “Tip Loss Factor Effects on Aerodynamic Performances of Horizontal Axis Wind Turbine,” *Energy Procedia*, vol. 118, no. April, pp. 136–140, 2017, doi: 10.1016/j.egypro.2017.07.028.

[78] C. G. Helmis, K. H. Papadopoulos, D. N. Asimakopoulos, P. G. Papageorgas, and A. T. Soilemes, “An experimental study of the near-wake structure of a wind turbine operating over complex terrain,” *Sol. Energy*, vol. 54, no. 6, pp. 413–428, 1995, doi: 10.1016/0038-092X(95)00009-G.

[79] L. J. Vermeer, J. N. Sørensen, and A. Crespo, “Wind turbine wake aerodynamics,” *Prog. Aerosp. Sci.*, vol. 39, no. 6–7, pp. 467–510, 2003, doi: 10.1016/S0376-0421(03)00078-2.

[80] J. Højstrup, “Spectral coherence in wind turbine wakes,” *J. Wind Eng. Ind. Aerodyn.*, vol. 80, no. 1–2, pp. 137–146, 1999, doi: 10.1016/S0167-6105(98)00198-6.

[81] J. H. Cheon and S. W. Lee, “Winglet geometry effects on tip leakage loss over the plane tip in a turbine cascade,” *J. Mech. Sci. Technol.*, vol. 32, no. 4, pp. 1633–1642, 2018, doi: 10.1007/s12206-018-0318-2.

[82] P. H. Madsen and S. Frandsen, “Wind-induced failure of wind turbines,” *Eng. Struct.*, vol. 6, no. 4, pp. 281–287, 1984, doi: 10.1016/0141-0296(84)90025-7.

[83] NASA, “Shape Effects on Drag,” *Department of Aerospace Engineering, California State University, Long Beach, California*, vol. 90840, pp. 1–1, 2007.

[84] C. V. Ram and R. S. Pant, “Multidisciplinary shape optimization of aerostat envelopes,” *J. Aircr.*, vol. 47, no. 3, pp. 1073–1076, 2010, doi: 10.2514/1.46744.

[85] P. González, W. Burgard, R. Sanz, and J. L. Fernández, “Developing a low-cost

autonomous indoor blimp," *J. Phys. Agents*, vol. 3, no. 1, pp. 43–52, 2009, doi: 10.14198/JoPha.2009.3.1.06.

[86] N. N. Efimev, "UNCLASSIFIED FUNDAMENTALS OF SUBMARINE THEORY Department of the Navy," 1966.

[87] U. S. N. Academy, "Course Objectives Chapter 10 Submarines and Submersibles," in *Principles of Ship performance*, Annapolis: United States Naval Academy, p. 30.

[88] San Francisco maritime national park Association, "The Trim System," San Francisco: San Francisco maritime national park Association, 2019, p. 18.

[89] M. F. Akorede, H. Hizam, and E. Pouresmaeil, "Distributed energy resources and benefits to the environment," *Renew. Sustain. Energy Rev.*, vol. 14, no. 2, pp. 724–734, Feb. 2010, doi: 10.1016/j.rser.2009.10.025.

[90] E. Hossain, E. Kabalci, R. Bayindir, and R. Perez, "A Comprehensive Study on Microgrid Technology," vol. 4, no. 4, p. 14, 2014.

[91] W. El-Khattam and M. M. A. Salama, "Distributed generation technologies, definitions and benefits," *Electr. Power Syst. Res.*, vol. 71, no. 2, pp. 119–128, Oct. 2004, doi: 10.1016/j.epsr.2004.01.006.

[92] L. Mariam, M. Basu, and M. F. Conlon, "Microgrid: Architecture, policy and future trends," *Renew. Sustain. Energy Rev.*, vol. 64, pp. 477–489, Oct. 2016, doi: 10.1016/j.rser.2016.06.037.

[93] A. Hirsch, Y. Parag, and J. Guerrero, "Microgrids: A review of technologies, key drivers, and outstanding issues," *Renew. Sustain. Energy Rev.*, vol. 90, pp. 402–411, Jul. 2018, doi: 10.1016/j.rser.2018.03.040.

[94] G. O. Suvire, P. E. Mercado, and L. J. Ontiveros, “Comparative analysis of energy storage technologies to compensate wind power short-term fluctuations,” in *2010 IEEE/PES Transmission and Distribution Conference and Exposition: Latin America (T&D-LA)*, Nov. 2010, pp. 522–528, doi: 10.1109/TDC-LA.2010.5762932.

[95] F. Díaz-González, A. Sumper, O. Gomis-Bellmunt, and R. Villafáfila-Robles, “A review of energy storage technologies for wind power applications,” *Renew. Sustain. Energy Rev.*, vol. 16, no. 4, pp. 2154–2171, May 2012, doi: 10.1016/j.rser.2012.01.029.

[96] P Barker,B Johnson, A Maitra, D Herman, “Investigation of the technical and economic feasibility of micro-grid-based power systems,” EPRI, Palo Alto, 2001.

[97] M. Drela, “Transonic low-Reynolds number airfoils,” *J. Aircr.*, vol. 29, no. 6, pp. 1106–1113, Nov. 1992, doi: 10.2514/3.46292.